

Illuminating the past 8 billion years of cold gas towards two gravitationally lensed quasars

J. R. Allison,¹★ V. A. Moss,^{2,3} J.-P. Macquart,^{3,4} S. J. Curran,⁵ S. W. Duchesne,⁵
E. K. Mahony,^{2,3} E. M. Sadler,^{2,3} M. T. Whiting,¹ K. W. Bannister,¹
A. P. Chippendale,¹ P. G. Edwards,¹ L. Harvey-Smith,¹ I. Heywood,^{1,6}
B. T. Indermuhle,¹ E. Lenc,^{1,2,3} J. Marvil,¹ D. McConnell¹ and R. J. Sault^{1,7}

¹CSIRO Astronomy and Space Science, PO Box 76, Epping NSW 1710, Australia

²Sydney Institute for Astronomy, School of Physics A28, University of Sydney, NSW 2006, Australia

³ARC Centre of Excellence for All-sky Astrophysics (CAASTRO)

⁴ICRAR/Curtin University, Curtin Institute of Radio Astronomy, Perth, WA 6845, Australia

⁵School of Chemical and Physical Sciences, Victoria University of Wellington, PO Box 600, Wellington 6140, New Zealand

⁶Department of Physics and Electronics, Rhodes University, PO Box 94, Grahamstown 6140, South Africa

⁷School of Physics, University of Melbourne, VIC 3010, Australia

Accepted 2016 November 3. Received 2016 November 2; in original form 2016 July 15

ABSTRACT

Using the Boolardy Engineering Test Array of the Australian Square Kilometre Array Pathfinder (ASKAP BETA), we have carried out the first $z = 0$ –1 survey for H I and OH absorption towards the gravitationally lensed quasars PKS B1830–211 and MG J0414+0534. Although we detected all previously reported intervening systems towards PKS B1830–211, in the case of MG J0414+0534, three systems were not found, indicating that the original identifications may have been confused with radio frequency interference. Given the sensitivity of our data, we find that our detection yield is consistent with the expected frequency of intervening H I systems estimated from previous surveys for 21-cm emission in nearby galaxies and $z \sim 3$ damped Lyman α absorbers. We find spectral variability in the $z = 0.886$ face-on spiral galaxy towards PKS B1830–211 from observations undertaken with the Westerbork Synthesis Radio Telescope in 1997/1998 and ASKAP BETA in 2014/2015. The H I equivalent width varies by a few per cent over approximately yearly time-scales. This long-term spectral variability is correlated between the north-east and south-west images of the core, and with the total flux density of the source, implying that it is observationally coupled to intrinsic changes in the quasar. The absence of any detectable variability in the ratio of H I associated with the two core images is in stark contrast to the behaviour previously seen in the molecular lines. We therefore infer that coherent opaque H I structures in this galaxy are larger than the parsec-scale molecular clouds found at mm-wavelengths.

Key words: galaxies: evolution – galaxies: high redshift – galaxies: ISM – quasars: absorption lines – galaxies: structure – radio lines: galaxies.

1 INTRODUCTION

The neutral interstellar medium (ISM) plays a fundamental role in galaxy evolution, providing the fuel available for star formation (e.g. Schmidt 1959; Kennicutt 1998) and the growth of supermassive black holes (see Heckman & Best 2014 for a review). Determining how the physical state of the neutral ISM in galaxies changes

over cosmological time-scales is therefore critical to our understanding of how these processes evolve throughout the history of the Universe. Neutral atomic hydrogen (H I) is typically abundant in gas-rich galaxies and readily detectable via either the 21-cm line in the nearby Universe or the Lyman α line at high redshifts. H I is therefore often used as a tracer of the neutral gas throughout the history of the Universe (see Wolfe, Gawiser & Prochaska 2005; Giovanelli & Haynes 2016 for reviews). However, the evolution of the H I mass density over cosmological time-scales (e.g. Zwaan et al. 2005; Martin et al. 2010; Braun 2012; Noterdaeme et al. 2012;

★ E-mail: james.allison@csiro.au

Zafar et al. 2013; Crighton et al. 2015; Sánchez-Ramírez et al. 2016) appears to be weaker by an order of magnitude than either the total star formation rate (e.g. Hopkins & Beacom 2006; Burgarella et al. 2013; Gunawardhana et al. 2013; Sobral et al. 2013; Zwart et al. 2014) or the molecular gas (e.g. Keres, Yun & Young 2003; Carilli & Walter 2013). It is therefore likely that the H I in galaxies represents a quasi-steady intermediate state between the warm ionized and cold molecular gas, with the latter responsible for directly fuelling star formation (e.g. Lagos et al. 2014). Although the H I may not directly trace the formation of stars in galaxies, understanding how its physical state, in particular the cold neutral medium (CNM; ~ 100 K), evolves over cosmological time will help elucidate its role in the formation of molecular gas and future star formation.

The present census of H I at intermediate cosmological redshifts ($z \approx 0.2$ – 1.7) is limited by significant observational challenges. The 21-cm line emission from individual galaxies is observationally expensive to detect with existing radio telescopes (see e.g. Catinella & Cortese 2015; Fernández et al. 2016) and cosmological work has focused on statistical detection through either stacking (e.g. Lah et al. 2007; Kanekar, Sethi & Dwarakanath 2016; Rhee et al. 2016) or intensity mapping (e.g. Chang et al. 2010; Masui et al. 2013). Likewise, the Lyman α line is only observable at ultraviolet (UV) wavelengths and necessitates the use of space-borne telescopes. Using the *Hubble Space Telescope* (HST), Rao, Turnshek & Nestor (2006) carried out a survey of damped Lyman α absorbers (DLAs; $N_{\text{HI}} \geq 2 \times 10^{20} \text{ cm}^{-2}$) through targeted observations of quasars with known strong Mg II absorption. They found that the DLA mass density showed little evolution between $z \approx 5$ and 0.5, but then must decrease by a factor of ≈ 2 in the past 5 Gyr to be consistent with results from 21-cm surveys. A more recent survey of the HST data by Neeleman et al. (2016) found a significantly lower incidence of DLAs when they accounted for the pre-selection biases due to targeting quasars with known metal absorbers and intervening galaxies. However, in both cases, fractional uncertainties are large due to the relatively small samples sizes involved, compared with nearby 21-cm surveys and larger optical DLA surveys at higher redshifts. We can instead use 21-cm absorption against suitably bright background radio sources to determine the abundance and kinematics of the H I. Furthermore, since 21-cm absorption is particularly sensitive to the cold gas, it is a powerful additional tool in surveying this phase of the H I at high redshift (Kanekar & Briggs 2004; Morganti, Sadler & Curran 2015).

In this paper, we present results from a 21-cm absorption survey for cold H I and OH gas towards two gravitationally lensed quasars – PKS B1830–211 at $z = 2.51$ (Lidman et al. 1999) and MG J0414+0534 at $z = 2.64$ (Lawrence et al. 1995) – covering intermediate cosmological redshifts between $z \approx 0$ and 1. We use commissioning data from the Boolardy Engineering Test Array (BETA; Hotan et al. 2014; McConnell et al. 2016) of the Australian Square Kilometre Array Pathfinder (ASKAP; Johnston et al. 2007; Schinckel et al. 2012). The relatively clean radio frequency environment and large fractional bandwidth available with this interferometer are particularly well suited to such a survey. Our choice of targets is based on the unique nature of the alignment between the radio source and at least one foreground galaxy. In both cases, the background quasar is strongly lensed into several compact image components, thereby creating multiple sight lines through each intervening system and so providing additional spatial information. Furthermore, the effect of any temporal behaviour in either the foreground galaxy or the background quasar will be magnified by the lensing system and is potentially detectable in the spectral line profile. Evidence for variability in extragalactic 21-cm absorp-

tion lines is rare and has only previously been found in the spectra of a few quasars (e.g. Wolfe, Briggs & Davis 1982; Kanekar & Chengalur 2001). These examples are attributed to either transverse motion of jet-knots in the background quasar (e.g. Briggs 1983) or interstellar scintillation (ISS) of a sufficiently compact background source or absorbing structure (e.g. Macquart 2005). The time-scales for spectral variability can then be used to infer the physical scale for optical depth variations in the absorbing H I gas.

H I absorption has been reported in the dominant lensing galaxy of each quasar (Chengalur, de Bruyn & Narasimha 1999; Curran et al. 2007), as well as several other possible intervening galaxies along the same sight line (e.g. Lovell et al. 1996; Curran et al. 2011; Tanna et al. 2013). In the case of MG J0414+0534, the number of intervening systems reported in the literature is far more than expected given the number density of DLAs estimated from large optical surveys (Tanna et al. 2013). However, flux ratios observed between the brightest image components at radio and mid-infrared wavelengths are inconsistent with a lens model based on just the detected optical counterparts, requiring a more complex mass distribution in the form of either satellite or intervening haloes and filaments (e.g. MacLeod et al. 2013; Inoue 2015). Therefore, by confirming whether there are indeed intervening H I systems, we hope that our data will help inform these alternative lens models.

We structure this paper as follows. In Section 2, we present a brief description of our observations and data analysis. We discuss our results for the two quasars in Sections 3 and 4. In Section 5, we estimate the expected number of intervening systems and discuss whether our results are consistent. We summarize our conclusions in Section 6.

2 OBSERVATIONS AND DATA

2.1 Observations with ASKAP BETA

During the period 2014 July to 2015 November, we carried out several observations of PKS B1830–211 and MG J0414+0534 with the ASKAP BETA telescope, which we summarize in Table 1. We followed a similar observing procedure to that described by Hotan et al. (2014) and McConnell et al. (2016), whereby focal-array primary beams were electronically formed to maximize the signal-to-noise ratio (S/N) towards nominal centre positions. Although the telescope can be used to form up to nine beams simultaneously for wide-field imaging, in this paper, we focus on a single beam formed towards the target quasar at the pointing centre. Observations of each quasar were accompanied by short (5–15 min) scans of PKS B1934–638 for initial calibration of the complex gains and setting the flux scale based on the model of Reynolds (1994).¹

Three frequency bands were used: 711.5–1015.5 MHz, 967.5–1271.5 MHz, and 1223.5–1527.5 MHz, spanning all H I redshifts between $z = 0$ and 1. We spent more observing time on the lowest frequency band, which covered most of the redshift interval, was least contaminated by radio frequency interference (RFI), and contained known absorption lines that we either wanted to confirm or monitor for variability. The number of available antennas varied between observations (see Table 1), but in general the full six-antenna BETA is sensitive to angular scales in the range 40 arcmin to 45 arcsec between 711.5 and 1527.5 MHz. Therefore, both the target quasars were spatially unresolved in all observations and could be treated as point-like radio sources. The ASKAP

¹ <http://www.atnf.csiro.au/observers/memos/>

Table 1. Summary of observations using the ASKAP BETA telescope. Each observation is assigned a unique scheduling block identification (SBID) number. t_{int} denotes the on-source integration time (averaged over antenna baselines and taking into account flagging). σ_{chan} is the median rms noise^a per 18.5 kHz channel as a percentage of the continuum (relevant for absorption detection). Note that the shortest baseline (AK01–AK03) is discarded during data processing (see Serra et al. 2015).

Source name	SBID	Date	MJD		Frequency band [MHz]	Antennas ^b	t_{int} [h]	σ_{chan} [per cent]
			Start	End				
PKS B1830–211	163, 165	2014 July 07	56845.447	56845.887	711.5–1015.5	1, 3, 6, 8, 15	9.0	0.14
	166, 167	2014 July 08	56846.429	56846.872	967.5–1271.5	3, 6, 8, 9, 15	8.4	0.13
	213	2014 July 11	56849.419	56849.627	1223.5–1527.5	1, 3, 6, 8, 9, 15	4.0	0.33
	2216	2015 July 24	57227.411	57227.536	711.5–1015.5	1, 3, 6, 8, 15	2.5	0.29
	2248	2015 July 29	57232.573	57232.807	711.5–1015.5	1, 3, 6, 8, 15	4.8	0.22
	2328	2015 August 08	57242.377	57242.757	967.5–1271.5	1, 6, 8, 15	7.2	0.19
	2640	2015 September 28	57293.483	57293.629	711.5–1015.5	1, 3, 6, 8, 15	2.4	0.30
	2655	2015 September 29	57294.442	57294.567	711.5–1015.5	1, 3, 6, 8, 15	2.5	0.28
	2716	2015 October 13	57308.371	57308.587	711.5–1015.5	1, 3, 6, 8, 15	3.8	0.24
	2747	2015 October 18	57313.194	57313.407	711.5–1015.5	1, 3, 6, 8, 15	4.2	0.23
	2789	2015 October 21	57316.192	57316.405	711.5–1015.5	1, 3, 6, 8, 15	4.3	0.23
	2898	2015 October 24	57319.376	57319.584	711.5–1015.5	1, 3, 6, 8, 15	3.5	0.25
	2925, 2927	2015 October 26	57321.408	57321.560	711.5–1015.5	1, 3, 6, 8, 15	2.4	0.31
	2936	2015 October 27	57322.303	57322.520	711.5–1015.5	1, 3, 6, 8, 15	4.0	0.24
	2950	2015 October 28	57323.426	57323.551	711.5–1015.5	1, 3, 6, 8, 15	2.0	0.34
	2973, 2974	2015 October 30	57325.288	57325.519	711.5–1015.5	1, 3, 6, 8, 15	4.2	0.23
MG J0414+0534	218	2014 July 12	56850.176	56850.237	711.5–1015.5	1, 3, 6, 8, 9, 15	1.3	1.8
	1544	2015 March 17	57098.279	57098.430	967.5–1271.5	1, 3, 8, 9, 15	2.5	1.4
	1545	2015 March 17	57098.433	57098.557	1223.5–1527.5	1, 3, 8, 9, 15	2.1	3.6
	1962, 1966	2015 June 16	57189.099	57189.267	711.5–1015.5	1, 6, 8, 15	2.7	1.9
	2225	2015 July 25	57228.838	57229.204	711.5–1015.5	1, 3, 6, 8, 15	6.9	0.76
	2231	2015 July 27	57230.815	57230.998	1223.5–1527.5	1, 3, 6, 8, 15	3.3	2.7
	2336	2015 August 10	57244.796	57245.110	967.5–1271.5	1, 6, 8, 15	5.6	1.2
	2340	2015 August 11	57245.830	57246.019	967.5–1271.5	1, 6, 8, 15	3.2	1.5
	2938	2015 October 27	57322.628	57322.786	711.5–1015.5	1, 3, 6, 8, 15	2.5	1.4
	2952	2015 October 28	57323.660	57323.944	711.5–1015.5	1, 3, 6, 8, 15	4.9	0.98
	2967	2015 October 29	57324.809	57324.942	711.5–1015.5	1, 3, 6, 8, 15	2.2	1.8
	3013	2015 November 03	57329.654	57329.928	711.5–1015.5	1, 3, 6, 8, 15	4.7	1.1
	3046	2015 November 06	57332.624	57332.921	711.5–1015.5	1, 3, 6, 8, 15	5.1	0.88
	3062	2015 November 08	57334.587	57334.794	711.5–1015.5	1, 3, 6, 8, 15	2.9	1.2

^aIn general, the noise scales as expected with the integration time and number of antennas. However, it should be noted that during commissioning, the sensitivity of ASKAP BETA did change between observations and was known to decrease significantly towards the higher frequencies (see e.g. McConnell et al. 2016).

^bSee figure 2 of Hotan et al. (2014) for details of the ASKAP BETA antenna positions.

BETA fine filterbank generated 16 416 spectral channels separated by approximately 18.5 kHz, equivalent to velocity resolutions in the range 3.6–7.8 km s^{−1} spanning the three frequency bands.

2.2 Data reduction

For calibration, flagging, and imaging of ASKAP BETA data, we followed a procedure similar to that described by (Allison et al. 2015, A15). The uncalibrated visibilities from the ASKAP correlator were recorded in measurement set format and so we used the CASA² package (McMullin et al. 2007) for initial flagging, averaging, and splitting of the data. To aid bandpass calibration, we split the full spectral resolution data into the intervals on which the primary beams were formed (4 and 5 MHz chunks). This has the additional benefit that the data could then be more efficiently processed using standard data reduction packages in a parallel computing environment. Separately, we produced a frequency-averaged data set spanning the entire 304 MHz band, which could then be used for forming high S/N continuum images for self-calibration. However, to

mitigate contamination from satellite- and aviation-generated RFI (seen at the higher frequencies included in this work), we increased the resolution of the averaged data from the 9.5 MHz bins used by A15 to 1 MHz.

All subsequent flagging, calibration, and imaging were carried out using standard tasks from the MIRIAD³ package (Sault, Teuben & Wright 1995). Automated flagging of corrupted data was achieved using an implementation of the SumThreshold method (Offringa et al. 2010) in the PGFLAG task, which for broad-band-RFI-free regions of the spectrum resulted in data loss of a few per cent. Observations of PKS B1934–638 were used to set the flux scale, based on the model of Reynolds (1994), and solutions for the complex gain were then copied across to the corresponding observation of the quasar. Further corrections to the time varying complex gains were calculated using several iterations of self-calibration on the full-band 1 MHz averaged data at successively smaller solution intervals. The initial model was constructed from the catalogue of the National Radio Astronomy Observatory Very Large Array Sky Survey (NVSS; Condon et al. 1998), followed by multifrequency

² <http://casa.nrao.edu>

³ <http://www.atnf.csiro.au/computing/software/miriad>

CLEAN component models constructed from imaging the data. The gain solutions were then transferred to all 4 and 5 MHz chunks of visibility data at full spectral resolution.

In the high S/N regime, an important aspect of achieving high dynamic range is a reliable method for accounting for the spectral behaviour of the continuum. To this end, we adapted the method used by A15 to improve the accuracy of the optical depth measurement. First, the CLEAN deconvolution algorithm was used to construct a continuum model of the field in each 4 and 5 MHz beam-forming interval. The target quasar was then masked and the model subtracted from the corresponding visibility data, effectively removing other bright sources in the field. We then used an adapted version of the UVLIN task to fit a second-order polynomial to the continuum, which was then divided out and a value of unity subtracted to form normalized continuum-subtracted visibilities. Importantly, this adapted method accounted for any gradient and/or curvature in the continuum⁴ which would contribute systematic error to our estimate of the optical depth in high S/N data. Imaging of the visibilities was carried out using the standard procedure with natural weighting to optimize the S/N for detecting absorption lines. We identified the centroid position of the quasar from the peak flux density in the averaged continuum image, and then extracted the spectra at this position from each normalized continuum-subtracted cube using MBSPECT.

2.3 Spectral analysis

We used three frequency bands in our observations, enabling a search for H I absorption spanning redshifts between $z = 0.0$ and 1.0 (or $z = 0.1$ and 1.3 for the 18 cm OH lines). For each of our target quasars, we generated a single composite spectrum by shifting the individual spectra to the common Solar barycentre rest frame and taking the variance-weighted arithmetic mean. The composite ASKAP BETA spectra are shown in Figs 1 and 2, where we have indicated those 21-cm H I and 18-cm OH lines previously reported in the literature. Approximately 14 per cent of the redshift coverage was rendered unavailable due to satellite and aviation generated RFI, predominantly at $z \lesssim 0.4$. We used the spectral line detection method discussed by Allison, Sadler & Whiting (2012), Allison, Sadler & Meekin (2014) to identify absorption lines in each spectrum, which performs multimodal nested sampling (Feroz & Hobson 2008; Feroz, Hobson & Bridges 2009) to calculate the probability of spectral lines in the data.

In several figures throughout this paper (e.g. Fig. 3), we compare our spectra with those in the literature, showing in each case the difference spectrum normalized by the rms noise. In order to account for the different resolutions and frequency sampling in each observation, we have smoothed and re-sampled (using cubic spline interpolation) each spectrum to a common resolution that is equal to the quadrature sum of the two individual resolutions. This process ensures that the frequency bins in the resulting difference spectrum are independent and can therefore be used to identify any significant deviations from zero. In the case of ASKAP BETA, the response of the 18.5 kHz channels (Tuthill et al. 2012) produces a correlation of only $\rho_{\text{chan}} \approx 4 \times 10^{-4}$ between adjacent channels and so we can

assume a spectral resolution equal to the channel spacing. For the other spectra taken from the literature, we have used the resolution information available from those publications.

3 PKS B1830–211

PKS B1830–211 is a well-studied radio-loud blazar at a redshift of $z = 2.51$ (Lidman et al. 1999) which is strongly gravitationally lensed by a foreground galaxy (e.g. Subrahmanyan et al. 1990; Jauncey et al. 1991; Nair, Narasimha & Rao 1993). At cm-wavelengths, the image comprises two compact flat-spectrum components, separated by approximately 1 arcsec and orientated to the north-east (NE) and south-west (SW) of the lens centre (e.g. Rao & Subrahmanyan 1988; Subrahmanyan et al. 1990), which are connected by an Einstein ring of steep-spectrum emission from the lensed jet (Jauncey et al. 1991). The spiral galaxy lens at $z = 0.886$ (Wiklind & Combes 1996) is rich in molecules, with over 40 different species detected so far, the majority of which are seen in absorption against the compact SW image of the core (see e.g. Muller et al. 2014 and references therein). H I absorption was also previously detected in both this (Chengalur et al. 1999; Koopmans & de Bruyn 2005) and a possible second intervening galaxy at $z = 0.192$ (Lovell et al. 1996).

The flux density of this source at cm-wavelengths (~ 10 Jy) makes it a perfect target for a line-of-sight survey for 21-cm H I and 18-cm OH absorption. Using commissioning data from ASKAP BETA, we have detected a total of three intervening systems between $z_{\text{HI}} = 0$ and 1, consisting of H I absorption in the Milky Way, H I, and OH absorption in the $z = 0.886$ galaxy, and probable H I absorption in a second intervening galaxy at $z = 0.192$. All three systems were previously reported in the literature and we detected no further intervening galaxies throughout the spectrum shown in Fig. 1. In the following, we discuss each of these systems in more detail.

3.1 Absorption in the galactic ISM

Strong H I absorption ($\tau_{\text{peak}} \approx 0.9$) is seen at 1420 MHz along the line of sight to PKS B1830–21, which passes within 2 kpc of the Galactic Centre and leaves the Solar circle on the far side at about 2 kpc below the Galactic plane ($b = -5^\circ 7'$, $l = 12^\circ 2'$). Originally reported by Subrahmanyan et al. (1992) using the Australia Telescope Compact Array (ATCA), several distinct velocity components can be seen in the line extending from approximately -15 to 100 km s^{-1} in the local standard of rest (LSR) velocity frame, tracing cold atomic gas from within 17 kpc of the Sun (positive velocities) to beyond the Solar circle (negative velocities). By identifying that the weak -9 km s^{-1} component was common to both the emission and absorption lines, Subrahmanyan et al. (1992) argued that PKS B1830–211 was likely located beyond the H I disc of the Milky Way and therefore extragalactic in origin. Notwithstanding that our ASKAP BETA data have lower spectral resolution (by a factor of approximately 2.5), we find that the bulk of this velocity structure is also seen in our data (Fig. 3).

Over the 23 yr interval spanned by the ASKAP BETA and ATCA data, it is possible that temporal variations in the line profile could arise from the motion of individual optical depth fluctuations transiting the quasar sight line. For example, in the case of absorbing gas on the far side of the Galactic Solar circle, we expect transverse velocities of up to $\sim 400 \text{ km s}^{-1}$ with respect to the quasar sight line (e.g. Reid et al. 2014), corresponding to a physical scale of $\sim 2000 \text{ au}$. At a distance of $\sim 17 \text{ kpc}$ from the Sun, this physical

⁴ Frequency-dependent features in the continuum can either be generated by intrinsic structure in the source spectrum, residual source-confusion or the instrumental band-pass. For example, we see a low-level 25 MHz-period ripple towards the low-frequency end of the band, which is caused by a standing wave between the dish and focal plane.

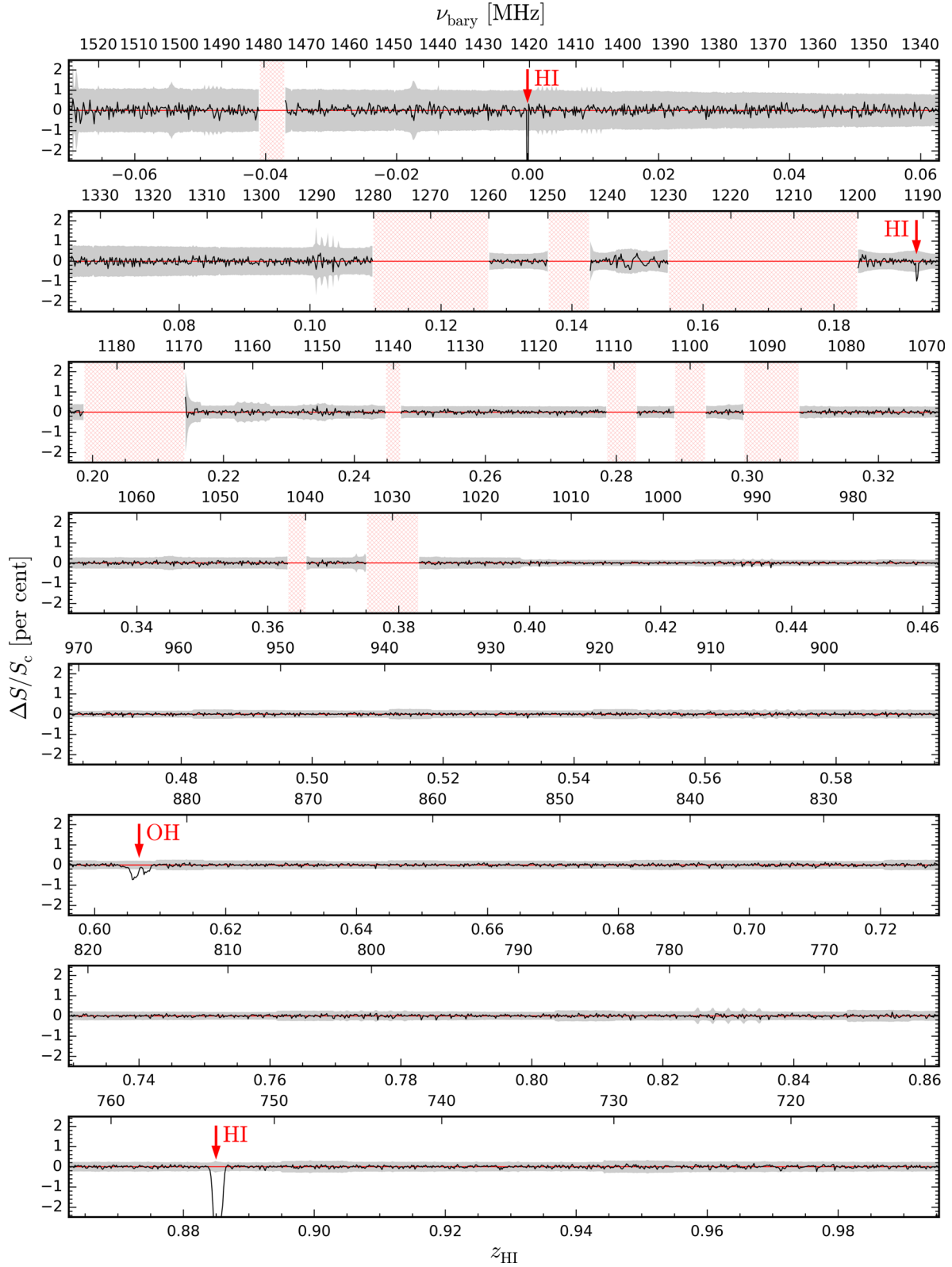


Figure 1. The final ASKAP BETA spectrum (averaged over all observations) towards PKS B1830–211. For visual clarity, the data have been binned by a factor of 3, from the native spectral resolution of 18.5 kHz to 55.6 kHz. The barycentric H I redshift is shown on the lower horizontal axis and the corresponding observed frequency is shown on the upper horizontal axis. The data (black line) denote the change in flux density (ΔS) as a percentage of the total continuum (S_c) and the grey region gives the corresponding rms spectral noise multiplied by a factor of 5. Prominent features in the noise are the result of individual failures in the beamformer or correlator cards for specific observations. The hatched regions mask data that were significantly contaminated by aviation and satellite-generated RFI. The red arrows indicate the positions of previously reported H I and OH lines.

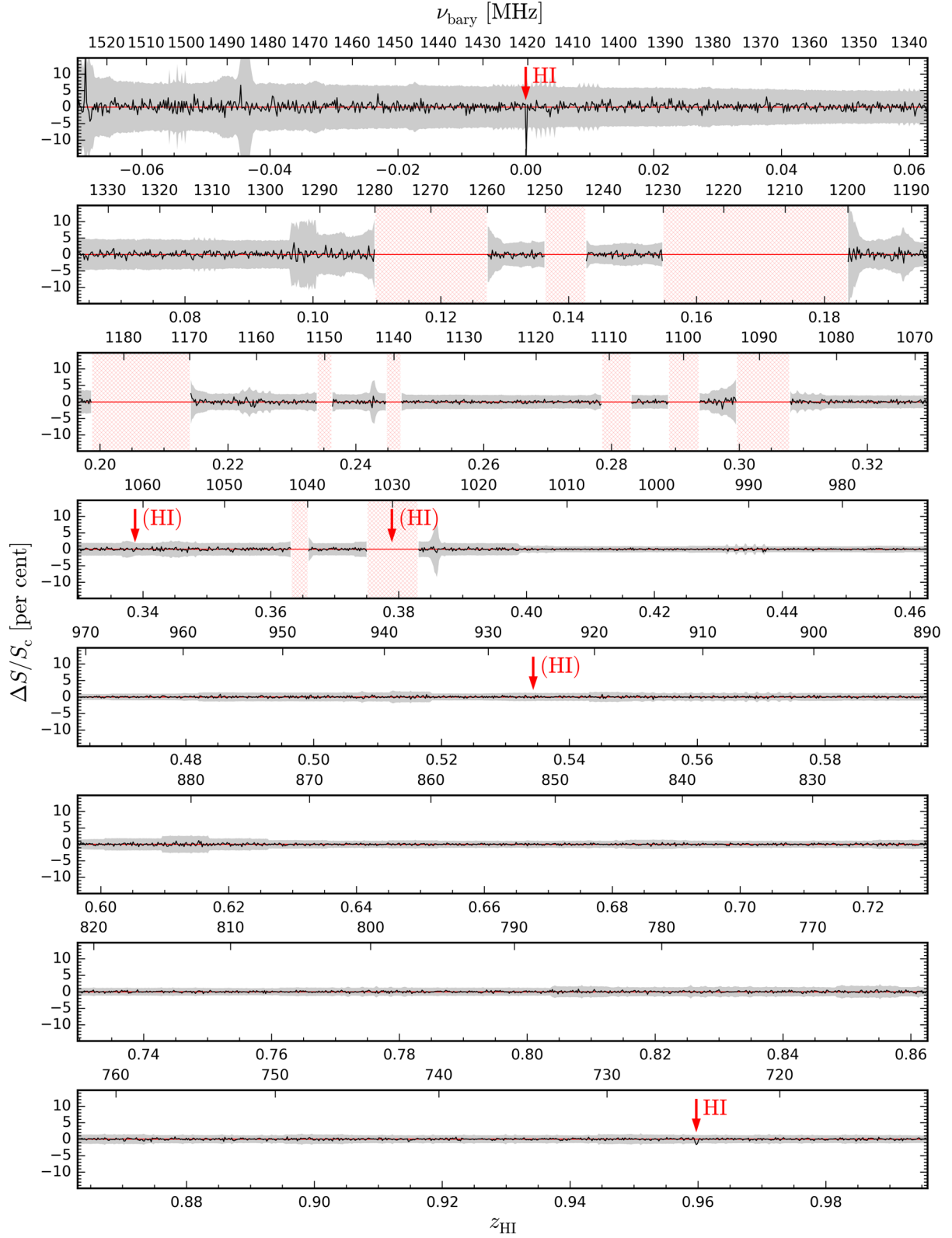


Figure 2. As Fig. 1, but showing the final spectrum for MG J0414+0534. Parentheses indicate those H I lines that were previously reported in the literature but were not detected in our data (see text for details).

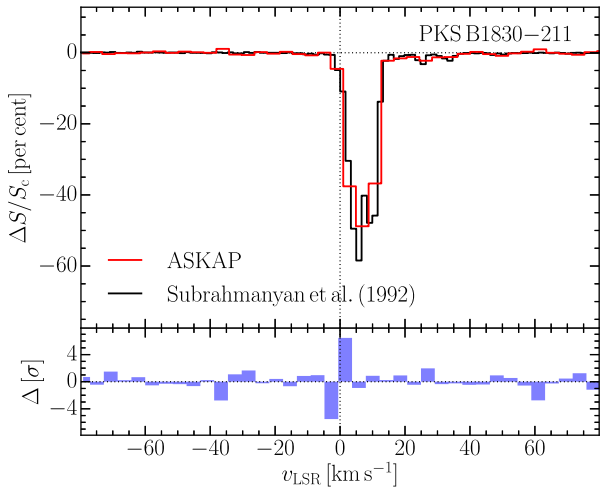


Figure 3. Spectra from ASKAP BETA (this work) and ATCA (Subrahmanyan, Kesteven & te Lintel Hekkert 1992) showing Galactic H I absorption towards PKS B1830–211. The difference spectrum (blue filled) is shown in the bottom panel. Although $\sim 6\sigma$ peaks are apparent in the difference spectrum, the line is not sufficiently sampled by the 18.5 kHz ASKAP BETA channels and we attribute these features to artefacts of the binning rather than temporal changes in the line-of-sight gas.

scale would equate to angular scales of ~ 0.1 arcsec. Although the entire extent of the source at cm-wavelengths is about 1 arcsec, at least 10 per cent of the flux density is contained within ~ 0.1 arcsec each of the compact NE and SW images of the quasar core (Jauncey et al. 1991; Lovell et al. 1996). Since the quasar sight line passes near to the Galactic Centre, images of the core at cm-wavelengths are significantly scatter broadened by the ISM (Jones et al. 1996) and their intrinsic sizes are likely to be smaller than this (e.g. Garrett et al. 1997). The NE and SW components are therefore sufficiently compact at cm-wavelengths to resolve 21-cm optical depth fluctuations on 2000 au scales at 17 kpc. Certainly transverse structures with significant 21-cm optical depths ($\Delta\tau \sim 0.1$ –1) have previously been reported on 10–1000 au scales (e.g. Johnston et al. 2003; Brogan et al. 2005; Goss et al. 2008; Lazio et al. 2009), and could arise naturally from a power spectrum of turbulent fluctuations in the ISM (e.g. Deshpande 2000; Roy et al. 2010, 2012; Dutta et al. 2014).

In Fig. 3, we show a comparison of our spectrum with that of Subrahmanyan et al. (1992), including the difference shown in the bottom panel (in units of the rms noise). The noise per 18.5 kHz channel in the ASKAP BETA spectrum is approximately a factor of five times that of the ATCA spectrum (at the same resolution) and is the dominant contributor to the rms noise in the difference spectrum. Since Subrahmanyan et al. (1992) measured a peak H I brightness temperature of approximately 50 K, we expect the noise to be higher on the line due to the contribution of H I emission to the system temperature (c.f. the 120 K system temperature expected off the line for ASKAP BETA; McConnell et al. 2016). However, we account for this by normalizing the difference spectrum based on the measured rms noise per channel. We see two features either side of $v_{\text{LSR}} = 0 \text{ km s}^{-1}$ that appear significant at a level $\sim 6\sigma$ and correspond to a change in 21-cm optical depth of $\Delta\tau \sim 0.05/c_f$, where c_f is the covering factor of the whole source. In the case of the NE and SW images of the core, these spectral features would then correspond to optical depth fluctuations equal to $\Delta\tau \sim 0.5$ (i.e. $c_f \sim 0.1$). Unfortunately, the absorption line is not well sampled by either the ASKAP BETA or ATCA data and so the difference spectrum is very sensitive to the re-sampling processes used for comparison.

We find that the apparent 6σ differences seen between the spectra are easily affected by changes in the binning. However, we suggest that future monitoring of this sight line at higher spectral resolution with ASKAP (see e.g. Dickey et al. 2013) could potentially reveal optical depth variations due to transverse motion of the small-scale Galactic CNM.

3.2 Intervening galaxies

3.2.1 The spiral galaxy lens at $z = 0.886$

So far more than 40 high-redshift absorption lines have been detected in the radio and sub-mm spectrum towards PKS B1830–211 due to an intervening galaxy at $z = 0.886$ (see Muller et al. 2014 and references therein). The spatial extent and velocity distribution of the gas inferred from absorption against the lensed structure of the source are consistent with a massive early-type spiral galaxy that is near to face on with respect to the line of sight (Wiklind & Combes 1998; Chengalur et al. 1999; Koopmans & de Bruyn 2005). This interpretation is supported by optical imaging using the *HST* that confirmed a spiral galaxy with clearly delineated spiral arms (Courbin et al. 2002; Winn et al. 2002). One of the spiral arms appears to intercept the SW core image where several saturated molecular absorption lines are detected (e.g. Frye, Welch & Broadhurst 1997; Muller et al. 2011).

In Fig. 4, we show the H I absorption line associated with this galaxy. Two distinct velocity components are evident and can be equated with gas at the positions of the NE (-150 km s^{-1}) and SW (0 km s^{-1}) core images (e.g. Chengalur et al. 1999). The full width of the line spans almost 400 km s^{-1} and is consistent with a low-inclination H I disc obscuring the entire image of the radio source, including the steep spectrum Einstein ring seen at 21-cm wavelengths. The inferred column density of $N_{\text{H I}} \gtrsim 2 \times 10^{21} \text{ cm}^{-2}$ (assuming $T_{\text{spin}} \gtrsim 100 \text{ K}$) is consistent with the disc of a large dusty spiral galaxy. By simultaneously fitting the 21-cm spectrum and a spatially resolved VLBI image of the continuum, Koopmans & de Bruyn (2005) showed that the absorption line could be modelled using a constant-velocity axisymmetric rotational disc with a radially dependent 21-cm optical depth. They estimated an inclination angle ($i \approx 17^\circ - 32^\circ$) that is consistent with the orientation inferred from the earlier radio and optical data, and a velocity dispersion ($\Delta v \approx 39\text{--}48 \text{ km s}^{-1}$) that is similar to that measured for the molecular lines (e.g. Wiklind & Combes 1996). The approximately 2:1 ratio of the NE and SW components in the line is consistent with an optical depth that increases with galactocentric radius and the closer proximity of the SW core to the H I-depleted centre (constrained by lens models; e.g. Kochanek & Narayan 1992; Nair et al. 1993).

Using the ASKAP BETA telescope, we monitored this line for 13 epochs during 2014 and 2015 in order to test for variability over the period spanned by our observing campaign and previous observations undertaken with the Westerbork Synthesis Radio Telescope (WSRT) almost 20 yr earlier (Chengalur et al. 1999; Koopmans & de Bruyn 2005). In Fig. 4, we compare each epoch to the average ASKAP BETA spectrum, and find that the H I absorption appears to vary on time-scales of approximately 1 yr. We discuss these results further in Section 3.3, but note here that the stability of the ASKAP BETA spectra obtained for all observing epochs during 2014 and 2015 is very encouraging for future H I absorption surveys with this telescope.

We also detect both of the 1665 and 1667 MHz main doublet lines of OH in absorption (see Fig. 5), originally reported by Chengalur et al. (1999). The line strength is approximately in the 9:5

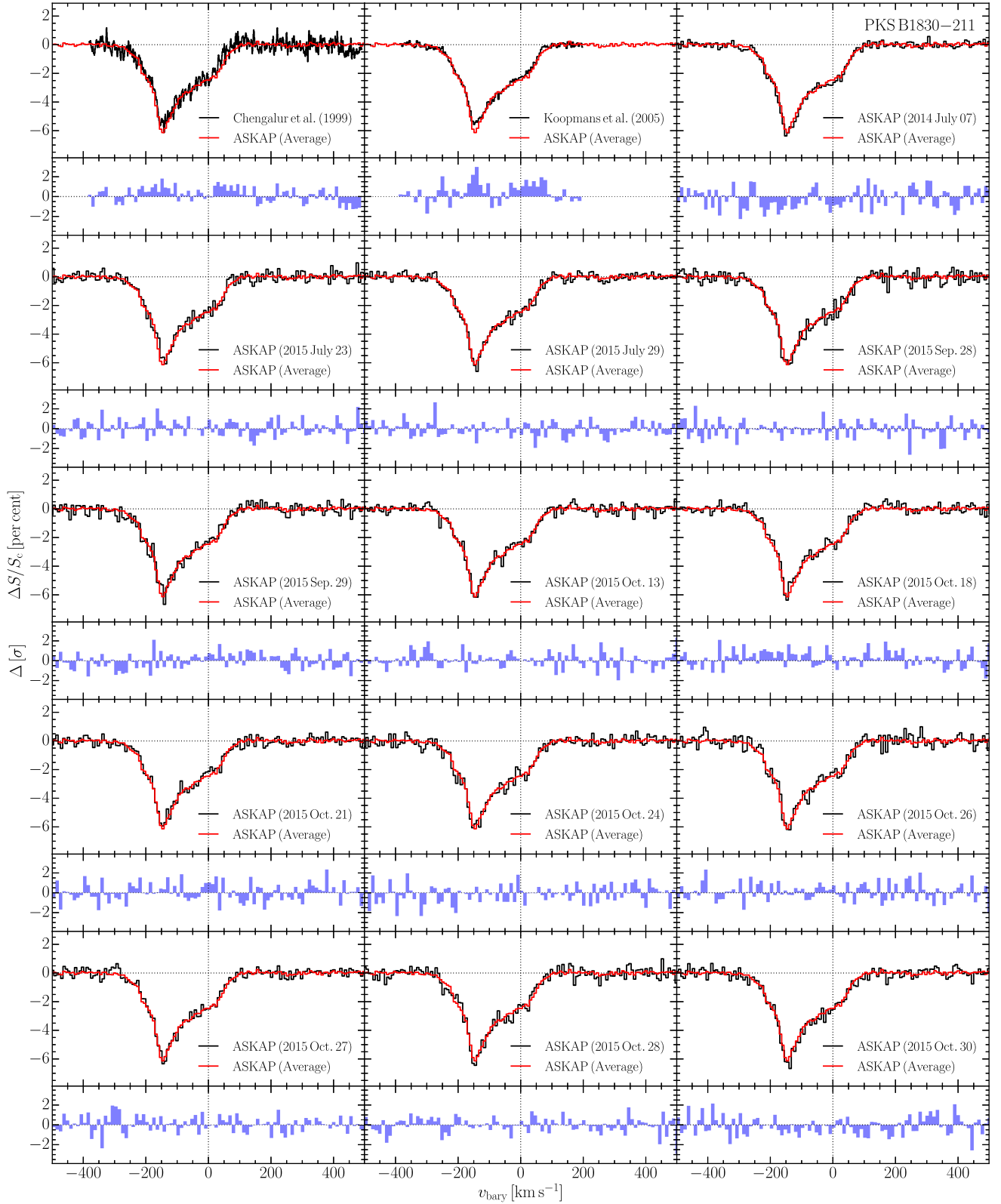


Figure 4. Spectra showing H I absorption arising in the face-on spiral galaxy at $z = 0.885, 82$ towards PKS B1830–211. The red line in each panel is a variance-weighted arithmetic mean of the data from all observations with the ASKAP BETA telescope over the period 2014–2015. A total of 15 epochs are shown, including two previous observations using the WSRT in 1997 (Chengalur et al. 1999) and 1998 (Koopmans & de Bruyn 2005). The difference spectra (blue filled) are shown in the panels below each epoch.

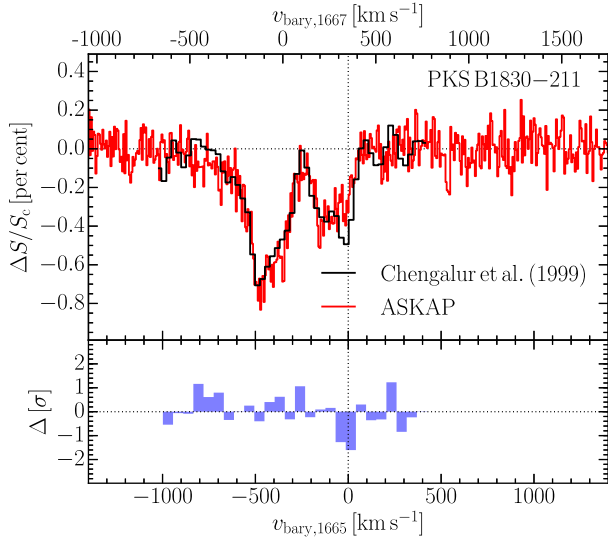


Figure 5. Spectra from ASKAP BETA (this work) and WSRT (Chengalur et al. 1999) showing the 1665 and 1667 MHz OH absorption lines at $z = 0.88582$ towards PKS B1830–211. The lower and upper velocity scales are given for the 1665 and 1667 MHz lines, respectively. The difference spectrum (blue filled) is shown in the bottom panel.

ratio expected from optically thin thermalized OH. If we assume a constant excitation temperature, then we would also expect to see the 1612 and 1721 MHz satellite lines at an optical depth of approximately 0.08 per cent. At the redshifted frequencies of these lines (855 and 912 MHz), the rms optical depth sensitivity of our data per 18.5 kHz channel is approximately 0.07 per cent. Assuming a line width of $\sim 50 \text{ km s}^{-1}$, our data would be sensitive to the satellite lines at the level $\sim 3\sigma$ and so non-detection is probably still consistent with thermalized OH, but future deeper observations should provide either detections or stronger constraints on departure from this assumption. The widths of the main lines suggest that the OH is widespread throughout the galactic disc, covering continuum emission from both the NE and SW core images and the Einstein ring. We find no significant evidence for optical depth variation between the 1665 and 1667 lines suggested by Chengalur et al. (1999); both lines appear to have higher absorption by a factor ~ 2 at -150 km s^{-1} compared with 0 km s^{-1} . This is similar to the ratio for the H I components and different to the other molecular absorption lines in this galaxy (e.g. Muller et al. 2011), where absorption against the NE image of the core is typically weaker than its SW counterpart. A likely scenario is that the OH absorption is tracing a more diffuse molecular component than spectral-line tracers of denser gas seen at mm-wavelengths. No significant variability is detected in the OH line, over the 20 yr time interval spanned by the ASKAP BETA and WSRT data, although the S/N is significantly lower than that of the H I line.

3.2.2 A possible second galaxy at $z = 0.193$

A further absorption line at 1190 MHz was discovered by Lovell et al. (1996) using the Parkes 64-m radio telescope, which they then confirmed following observations using the Australia Telescope Compact Array (ATCA) and four antennas of the Australian Long Baseline Array (LBA). Based on the relatively strong absorption against the NE image, in contrast to molecular absorption lines detected at $z = 0.886$, and the lack of common transitions known to exist at 2246 MHz (but see also Wiklind & Combes 1998), they

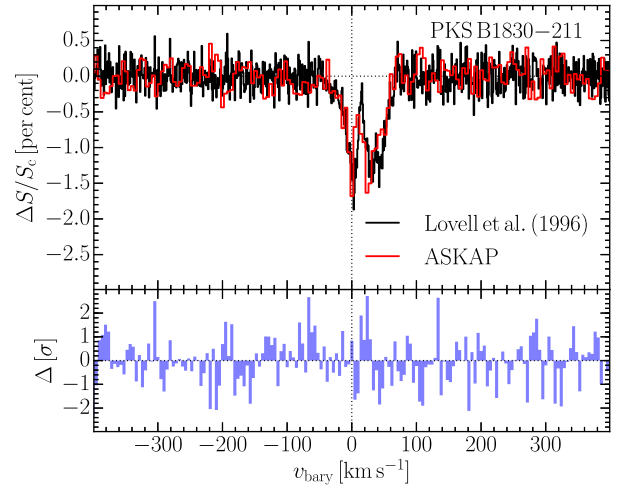


Figure 6. Spectra from ASKAP BETA (this work) and ATCA (Lovell et al. 1996) showing H I absorption associated with the possible intervening galaxy at $z = 0.1926$ towards PKS B1830–211. The difference spectrum (blue filled) is shown in the bottom panel.

argued that this line was associated with a second intervening H I absorber at a redshift of $z = 0.193$. The implied column density $N_{\text{H I}} \sim 10^{21} \text{ cm}^{-2}$ (assuming $T_{\text{spin}} \approx 100 \text{ K}$; Frye et al. 1997) is typical of a large spiral galaxy. A possible optical counterpart was found in the *HST* images of PKS B1830–211 by Courbin et al. (2002) and Winn et al. (2002), providing further evidence of a second intervening spiral galaxy. However, there is yet to be spectroscopic confirmation at either optical or sub-mm wavelengths (Muller et al. 2011). With ASKAP BETA, we confirm the existence of the 1190 MHz line and, at a 5σ optical depth sensitivity of 0.16 per cent (assuming a line width of $\sim 50 \text{ km s}^{-1}$), the absence of any corresponding absorption line at 1016 MHz (Fig. 1), supporting the argument that the 1190 MHz line is more likely to be H I than OH. At 1396 and 1398 MHz (where one might expect to detect the main OH doublet lines), the 5σ optical depth sensitivity of our data is only 0.46 per cent, giving a decidedly non-informative upper limit of ~ 3 for the H I to OH ratio. We find good agreement between the line profile in the ASKAP BETA spectrum and that of Lovell et al. (1996), recovering the two distinct components associated with gas (possibly in $\sim \text{kpc}$ spiral arms) that cover the NE core and Einstein ring components of the radio source (Fig. 6). At the S/N limit of the data, we find no evidence for any changes in the spectrum over the 20 yr time interval between these observations.

3.3 Spectral variability in the gravitational lens

Upon visual inspection of the difference spectra, shown in Fig. 4, it is apparent that the H I line in the $z = 0.886$ absorber towards PKS B1830–211 varies significantly above the noise. This is particularly clear when we compare the average ASKAP BETA spectrum with two published spectra from previous observations undertaken with the WSRT in 1997 (Chengalur et al. 1999) and 1998 (Koopmans & de Bruyn 2005).⁵ Koopmans & de Bruyn (2005) also noted seeing differences between the WSRT spectra, but as yet these have

⁵ Note that we have corrected the baseline for the Koopmans & de Bruyn (2005) spectrum by fitting and subtracting a linear component. We found that the baseline in the published spectrum appeared to deviate from zero by up to 0.13 per cent of the continuum.

not been published. Absorption line variability can be used to infer the scale of optical depth variations in foreground absorbing gas not normally possible with conventional imaging techniques. Mechanisms driving variability on day to year time-scales arise either from the apparent superluminal motion of beamed jet-knots in the background source (e.g. Briggs 1983), ISS of either sufficiently compact components of the continuum source or the absorbing region (e.g. Macquart 2005), or microlensing by small-scale changes in the foreground mass distribution (e.g. Lewis & Ibata 2003). It is plausible that changes in the physical properties of the absorbing gas can also drive variability. For example, Wolfe et al. (1982) claimed that if the excitation (spin) temperature is coupled to a nearby source of 21-cm continuum emission, which varies strongly, then detectable variation in the 21-cm optical depth would be possible.

Only a few examples of H I absorption variability have been reported in the literature so far. Notably, Wolfe et al. (1982) found significant changes in four narrow absorption components in the 21-cm spectrum of BL Lacertae object AO 0235+164, with durations of several months. Although the original data gave contradictory evidence in support of either intrinsic or extrinsic source models for the variability (see also Briggs 1983), ultimately subsequent optical spectroscopic confirmation of the source redshift (Cohen et al. 1987) conclusively favoured the latter scenario. A second variable 21-cm absorber was found by Kanekar & Chengalur (2001) in the DLA system towards the quasar PKS B1127–145, with a characteristic time-scale of a few days. Since there was no apparent correlation in the source and line flux densities, the authors favoured models with transverse motion of a knot in the background quasar, which possibly scintillates from either the Galactic and/or absorber ISM. The spectral variability that we see for the H I absorber in the PKS B1830–211 lens is therefore a rare example of 21-cm variability and its unique nature as a strongly lensed source may reveal new behaviour.

3.3.1 Modelling the spectral variability

By parametrizing spectral variability in terms of the equivalent width (EW), we can separate intrinsic changes in the optical depth and geometry of the absorber–source system from simple systematic errors or variations in the absolute flux density. In Fig. 7 we show, as a function of observing epoch, the total cm-wavelength continuum flux density, the EWs of the whole H I line, the NE and SW components, and their ratio. We avoid possible model-dependent artefacts that could result from fitting analytical profiles by measuring EW directly from the data shown in Fig. 4, over velocity channels spanning the absorption line. To detect any relative changes in absorption across the lensed radio image, we also consider absorption separately against the bright NE and SW components of the core by integrating sections of the line centred at -150 and 0 km s^{-1} (with respect to $z = 0.88582$) over a velocity width of $\Delta v = \pm 40 \text{ km s}^{-1}$, equal to the line broadening given by the model of Koopmans & de Bruyn (2005).

We employ a simple quantitative test by modelling the residual variability as a purely stochastic process that is independent between time samples and has a normal distribution of standard deviation σ_{vrb} . Although the assumption of independence is weak, we can nevertheless test for any residual deviation from a given temporal model (\mathcal{M}), above that expected from just the noise.⁶ The likelihood

of σ_{vrb} assuming a normal distribution for the data is then given by

$$\begin{aligned} \mathcal{L}(\sigma_{\text{vrb}}) &\equiv p(\mathbf{d}|\sigma_{\text{vrb}}, \sigma_{\text{noise}}, \mathcal{M}), \\ &= \int \frac{\pi(\boldsymbol{\theta})}{\sqrt{(2\pi)^N \prod_i \sigma_{\text{total},i}^2}} \exp \left[-\frac{1}{2} \sum_i \frac{(d_i - \mu_i(\boldsymbol{\theta}))^2}{\sigma_{\text{total},i}^2} \right] d\boldsymbol{\theta}, \end{aligned} \quad (1)$$

where

$$\sigma_{\text{total},i}^2 = \sigma_{\text{noise},i}^2 + \sigma_{\text{vrb}}^2, \quad (2)$$

\mathbf{d} is the set of measured data $[d_i, \dots, d_N]$, $\boldsymbol{\mu}$ are the expected values $[\mu_i, \dots, \mu_N]$ assuming a model \mathcal{M} defined by the parameters $\boldsymbol{\theta}$ with prior probability $\pi(\boldsymbol{\theta})$, and σ_{noise} are the expected standard deviations $[\sigma_{\text{noise},i}, \dots, \sigma_{\text{noise},N}]$ estimated from the measured rms for each observation. We can then compute the posterior probability density $p(\sigma_{\text{vrb}}|\mathbf{d}, \sigma_{\text{noise}}, \mathcal{M})$ by taking the product of $\mathcal{L}(\sigma_{\text{vrb}})$ and a suitable prior density function $\pi(\sigma_{\text{vrb}})$. We assume a priori ignorance of the value of σ_{vrb} and adopt the following scale-invariant Jeffreys' prior

$$\pi(\sigma_{\text{vrb}}) = \begin{cases} [3 \ln(10) \sigma_{\text{vrb}}]^{-1}, & \text{if } 10^{-3} \leq \sigma_{\text{vrb}}/\langle \mu \rangle < 1, \\ 0, & \text{otherwise.} \end{cases} \quad (3)$$

where we scale to $\langle \mu \rangle$, the mean of our data model. For the general class of models \mathcal{M} , we estimate $p(\sigma_{\text{vrb}}|\mathbf{d}, \sigma_{\text{noise}}, \mathcal{M})$ and its integral (Bayes factor) using PyMultiNest (Buchner et al. 2014), which implements the MultiNest algorithm (Feroz & Hobson 2008; Feroz et al. 2009, 2013).

In the first instance, we consider a model that is time independent so that all $\mu_i = \langle \mu \rangle$, the maximum likelihood of $\langle \mu \rangle$ simply being equal to the noise-weighted mean of the data. We show in Fig. 7 the median and 68.3 per cent credible interval for $\langle \mu \rangle$ and in Fig. 8 the marginalized posterior probability distribution for $\sigma_{\text{vrb}}/\langle \mu \rangle$. We calculate 99.7 per cent (3σ) credible intervals for $\sigma_{\text{vrb}}/\langle \mu \rangle$ of 1.5–7.5 per cent in the total EW, 1.7–8.5 per cent in the NE component, and 1.5–13.4 per cent in the SW component. By integrating the marginal posterior probability distribution over all $\sigma_{\text{vrb}}/\langle \mu \rangle$, and dividing by the posterior for the noise-only model, we calculate variability-to-noise-only Bayes factors of $\sim 3 \times 10^7$ in the total EW, $\sim 1 \times 10^7$ in the NE component, and $\sim 1 \times 10^3$ in the SW component, equivalent to two-model probabilities of 99.999 997, 99.999 991, and 99.91 per cent. Although there is clearly overwhelming evidence for variability in the EW, above that expected from just the measured noise, we find no evidence of variability in the ratio of the NE and SW components; $\sigma_{\text{vrb}}/\langle \mu \rangle$ is consistent with zero and has a 99.7 per cent (3σ) upper limit of 6 per cent, a Bayes factor of 0.38 and a two-model probability of 28 per cent. So while the H I EW varies at the level of a few per cent on yearly time-scales, it does so in a manner that is apparently coherent between the NE and SW components. This implies that the variability we see in the H I line is coupled to intrinsic brightening and fading of the core rather than any ISS or microlensing, which should produce independent variability in these two components.

We verify this interpretation by testing for a positive correlation between temporal variations in the total continuum flux density and the EWs of the line components. We construct a second model based on a cubic spline interpolation of the temporal behaviour in the total continuum flux density (assuming a spectral index of approximately zero over these frequencies), and then fit this to the H I EW data with a linear scaling and offset. The results are shown in Fig. 7 and we obtain linear scalings between the continuum and EWs of the total H I, NE, and SW components equal to $0.24^{+0.08}_{-0.11}$.

⁶ This approach has been used for other applications, see for example Purcell et al. (2015)

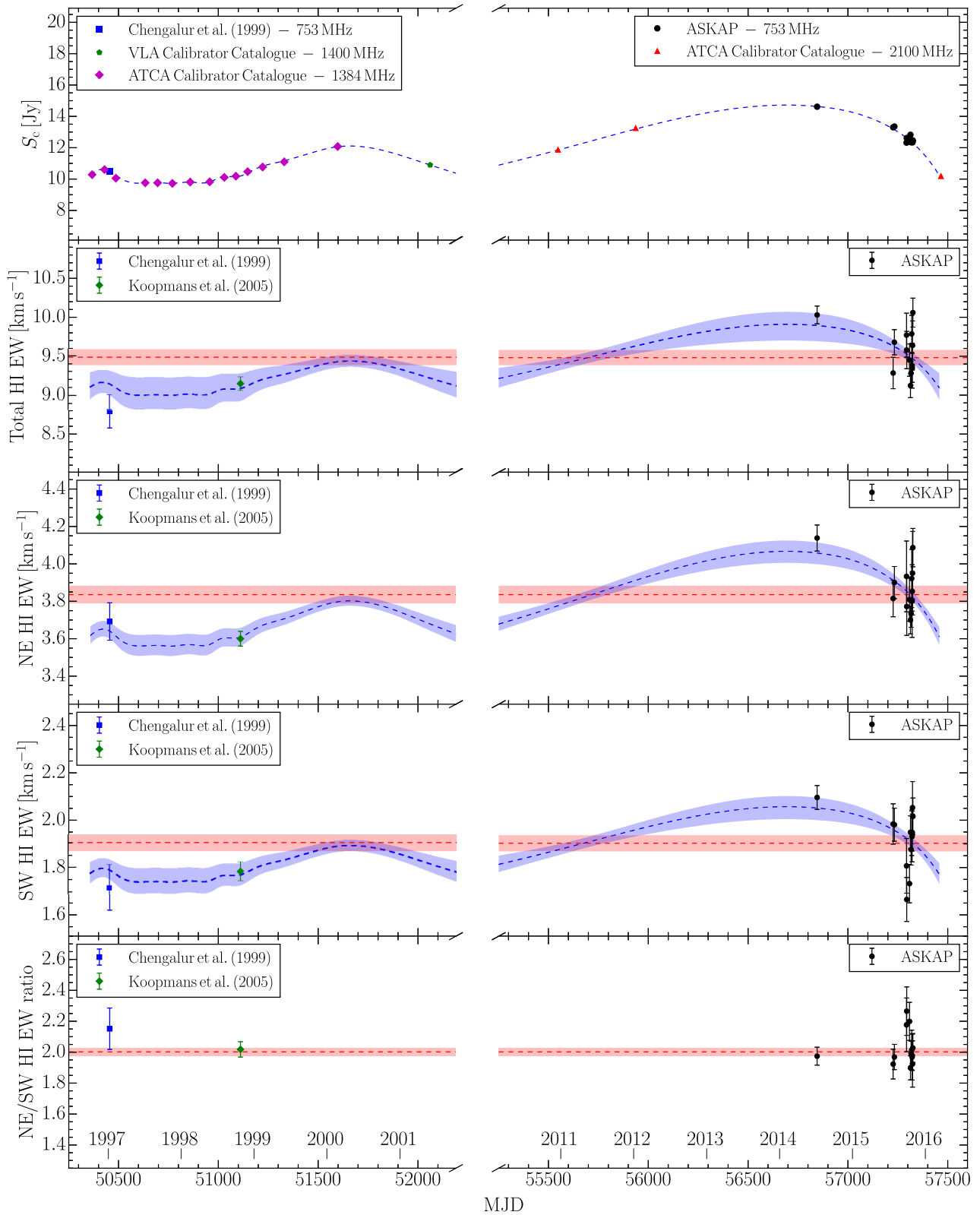


Figure 7. Time-series data for the total source flux density (top panel), EWs of the H I line, NE and SW components (middle panels), and their ratio (bottom panel), for the intervening spiral galaxy at $z = 0.88582$ towards PKS B1830–211. The results of model fitting are denoted by dashed lines (the median) and filled regions (68.3 per cent credible interval), where red models represent constant behaviour with respect to time and blue models are based on a cubic spline interpolation in the continuum data. The blue models are fit to the EW data using an offset and scaling parameter.

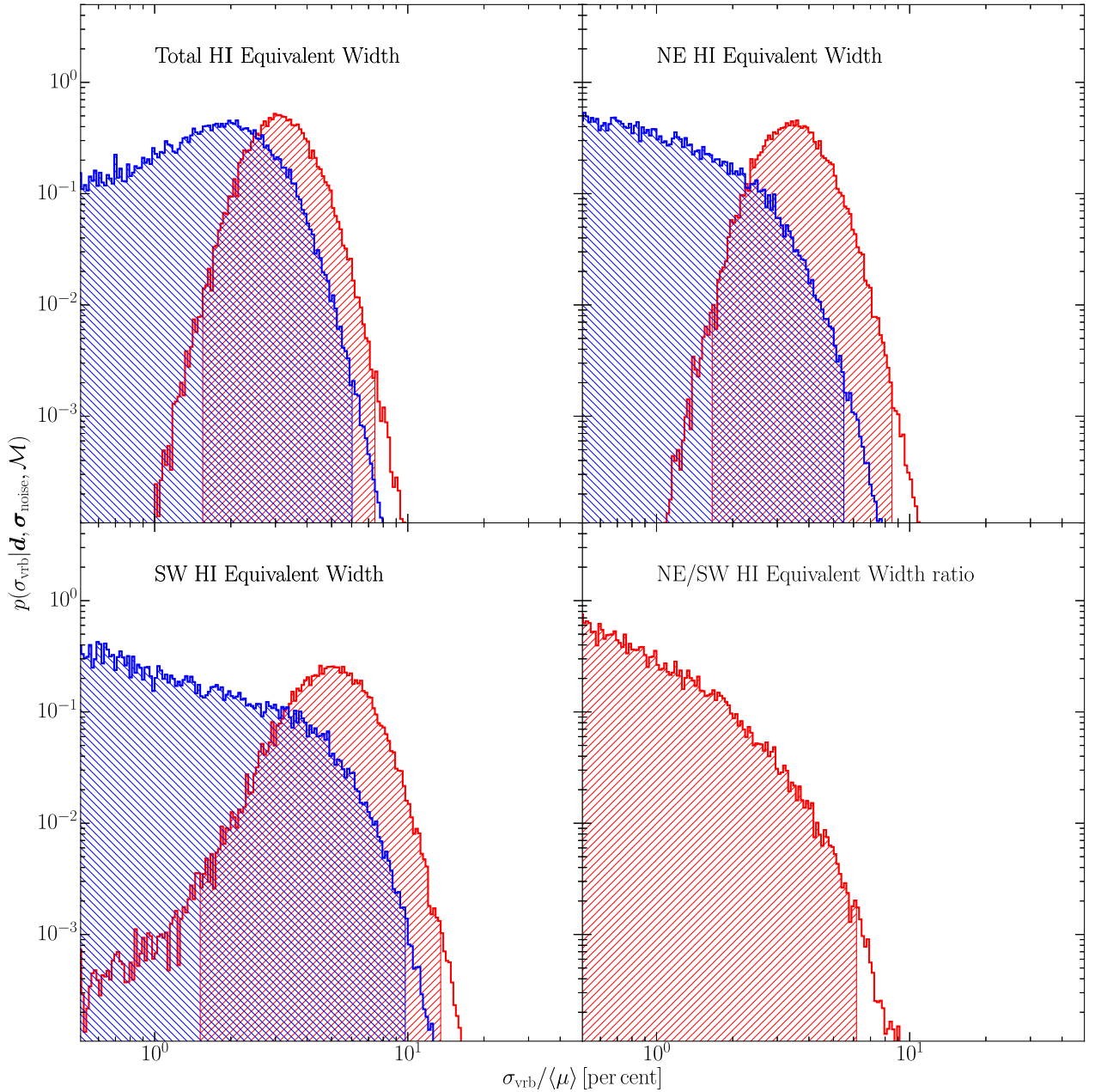


Figure 8. Marginal posterior probability distributions for fractional residual variability ($\sigma_{\text{vrb}}/\langle\mu\rangle$) in the EWs of the H I line, the NE and SW components, and their ratio. The bounded hatched regions represent the 99.7 per cent (3σ) credible interval about the distribution median. The red and blue distributions correspond to the two models (\mathcal{M}) shown in Fig. 7.

$0.33^{+0.06}_{-0.07}$, and $0.42^{+0.11}_{-0.13}$, respectively. The marginal posterior probability distributions for any residual variability are shown in Fig. 8 and we find no evidence for residual variability in either the NE or SW components of the line, with probabilities of 36 and 38 per cent, respectively. There is weak evidence for variability in the total EW with a probability of 77 per cent, which may indicate that a more complex model beyond a simple linear relationship is required, or that further variability is being driven by another process such as ISS.

Correlated variability naturally arises between the background flux density and EW of the H I line as a direct consequence of changes in the source brightness distribution. Consider an element

of optical depth τ_i and velocity width Δv_i , obscuring a component S_i of the background continuum S_c . The EW of this element is then given by

$$\text{EW}_i \approx \frac{S_i}{S_c} (1 - e^{-\tau_i}) \Delta v_i. \quad (4)$$

If we assume that the optical depth does not change significantly on the time-scales sampled by our data, then we derive the following relationship between fractional changes in the EW and the total continuum

$$\frac{\delta \text{EW}_i}{\text{EW}_i} \approx \left(\frac{f'_i}{f_i} - 1 \right) \frac{\delta S_c}{S_c}, \quad (5)$$

where $f_i = S_i/S_c \leq 1$ and $f'_i = \delta S_i/\delta S_c \leq 1$. Fractional changes in EW_i and S_c are positively correlated if $f'_i > f_i$, i.e. the source preferentially brightens or fades in this component. In the case of PKS B1830–211, we find that fractional changes in the EWs that are nominally associated with the NE and SW core images are ~ 30 per cent that of the total continuum, from which we can infer that no more than ~ 75 per cent of the total continuum is contained in these components (consistent with imaging). The inequality comes about because we cannot, in practice, resolve individual components in the H I absorption line (which have a typical width $\sim 40 \text{ km s}^{-1}$; Koopmans & de Bruyn 2005), and so there will be some contribution from non-varying components of the source. Under this model, we also expect the steep-spectrum Einstein ring not to vary on these time-scales (i.e. $f'_i = 0$) and so fractional changes in EW for this component should be 100 per cent anti-correlated with the total continuum flux density. The overall affect of these different components is to alter the shape of the H I line, which can be seen clearly in Fig. 4. A net positive correlation between the EW of the whole H I line and S_c indicates that the images of the core have a higher covering factor than the Einstein ring, perhaps due to the relative position of the inner H I-depleted disc and source (see e.g. Koopmans & de Bruyn 2005) or the extended nature of the ring.

In summary, we find that the EWs of the total, the NE and SW components of the H I line fluctuate at the level of a few per cent over yearly time-scales and are correlated with larger fractional variations in the total continuum flux density of the source. Over the same time-scale, there is no significant evidence of variability in the ratio of the NE and SW components of the H I line. This behaviour naturally arises if intrinsic variability in the core causes simultaneous changes in the NE and SW images (on time-scales larger than the known 25 d delay) and leads to differential changes in the source surface brightness distribution with respect to the absorbing H I gas. We propose that similar intervening H I lines that have two or more distinct and widely spaced ($\Delta v \sim 100 \text{ km s}^{-1}$) velocity components, and which exhibit correlated variability, should provide a reasonably strong prior for finding new gravitationally lensed quasar candidates.

3.3.2 A silhouette against intrinsic variability in the blazar jet

PKS B1830–211 is known to exhibit intrinsic high-energy variability that is typical of a luminous blazar, including several recently detected strong γ -ray flares (Barnacka, Glicenstein & Moudén 2011; Donnarumma et al. 2011; Abdo et al. 2015; Barnacka et al. 2015). Observations at mm wavelengths (e.g. Garrett et al. 1997; Jin et al. 2003; Muller & Guélin 2008) also reveal intrinsic variation in the flux densities of the NE and SW images of the core that is consistent with the formation of new synchrotron-emitting plasmons which are ejected at the base of the quasar jet. The ratio of these components is then modulated by a 25 d time delay at the gravitational lens (Lovell et al. 1998; Wiklind & Combes 2001; Barnacka et al. 2011, 2015). Evidence for intrinsic changes in the quasar core is further supported by mm-imaging of rapid (weekly and monthly) $\sim 100 \mu\text{as}$ -scale changes in the centroid separation and structure of these components (Garrett et al. 1997, 1998; Jin et al. 2003). Nair, Jin & Garrett (2005) proposed a helical model for the jet to explain this behaviour, with an observed doppler-boosted precession period of approximately 1 yr, which they suggested could be evidence for a binary supermassive black hole. More recent observations over a few months were carried out by Martí-Vidal et al. (2013) using the Atacama Large Millimetre Array (ALMA) and spanning frequencies between 100 and 300 GHz, revealing sub-mm flaring activity

that was concurrent with a particularly energetic γ -ray flare. Their work uncovered chromatic structure close to the base of the jet (a core-shift effect) for which they found that a concave-jet model of plasmon ejection could explain the observed frequency-dependent variation in the flux–density ratio between the two core images.

The simultaneous brightening and fading of the H I absorption that we find in the NE and SW components, correlated with variability in the total continuum flux density, is a direct consequence of the cumulative formation and eventual dissipation of optically thick plasmons at the base of the jet. Brightening of the core leads to an overall concentration of the total continuum flux density towards the NE and SW components, which then increases the EW we measure at these velocities at the expense of the non-variable steep-spectrum ring. We expect that further 21-cm line observations with ASKAP, at higher spectral S/N and cadences, would reveal the effect of the 25 d lens time delay in the NE/SW EW ratio.

3.3.3 Comparison with the molecular line variability

Similar long-term variability has also been observed in molecular absorption at mm-wavelengths. Muller & Guélin (2008) carried out monitoring between 1995 and 2007 of the HCO^+ (2-1) and HCN (2-1) lines at 3-mm using the IRAM Plateau de Bure interferometer (PdBI) and IRAM 30 m telescopes. During this period, they found significant, and correlated, variability in molecular absorption towards the NE and SW lens components and the total continuum flux density. As with the H I absorption, this behaviour is symptomatic of changes in the source brightness distribution. However, in contrast to the H I data presented here, they also found significant changes in the opacity ratio of the NE component and the blue-wing of the SW component, on time-scales much larger than that expected from the known 25 d lens time delay. Notably, they found a decrease of almost 50 per cent in the NE/SW ratio between 2003 and 2006, the direct result of a reduction in absorption against the NE component by more than a factor of 6. Given that the sub-structure of the imaged core is known to change on scales of more than $\sim 100 \mu\text{as}$ ($\sim 1 \text{ pc}$ at $z = 0.886$) at mm-wavelengths (e.g. Jin et al. 2003), over time-scales of several months to a year, Muller & Guélin (2008) proposed that this behaviour is the result of changes in the NE and SW sight lines through a sparse distribution of diffuse molecular clouds.

Molecular line variability has continued to be seen in subsequent observations of both the NE and SW source components. Muller et al. (2013) compared their ATCA 7-mm spectra from earlier observations in 2009 and 2010 obtained by Muller et al. (2011), and found significant differences for several species. Schulz et al. (2015) used the Effelsberg 100-m telescope at cm-wavelengths to monitor variability in CS (1-0) absorption towards the SW component, finding a striking similarity to the variations in HCO^+ (2-1) discovered by Muller & Guélin (2008). Recently, Muller et al. (2014) carried out a spectroscopic survey of common interstellar molecules using the ALMA. They detected short-term (~ 2 months) variations in the wings of the saturated CO (4-3), HCO^+ , and HCN (2-1) lines towards the SW image that were concurrent with the sub-mm counterpart to the γ -ray flare found by Martí-Vidal et al. (2013). They also compared their ALMA spectra with the previous ATCA 3 and 7-mm spectra (obtained by Muller & Guélin 2008; Muller et al. 2011, 2013), seeing again the approximately yearly variability in several other molecular species in addition to that in HCO^+ , HCN, and CS. However, it remains to be seen if the spectral variability seen in either the H I or molecular lines is periodic, as might be expected from the helical jet model proposed by Jin et al. (2003).

Relative changes in the NE and SW opacities of the molecular lines are consistent with optical depth variations that are well matched to ~ 1 pc-scale changes in the source structure at mm-wavelengths. The absence of similar variability in the H I NE/SW ratio implies that structural changes in the source at 21-cm wavelengths are not sensitive to fluctuations in the optical depth. This could be due to be the typical size on which coherent opaque H I structures are seen through the face-on disc of this galaxy, which would imply a transverse physical scale larger than a parsec. This would be consistent with high spatial-resolution imaging of several redshifted 21-cm absorbers, which typically imply sizes for coherent absorbing structures ranging from the 10 pc to kpc-scale (see e.g. Lane, Briggs & Smette 2000; Srianand et al. 2013; Borthakur et al. 2014; Biggs et al. 2016; Dutta et al. 2016). A detailed 21-cm study of the Local Group galaxies M31, M33, and LMC by Braun (2012) revealed self-opaque high- N_{HI} structures with typical sizes ~ 100 pc. Gupta et al. (2012) similarly concluded from their 21-cm survey of a large sample of Mg II absorbers towards compact quasars that the typical correlation length is ~ 30 – 100 pc. We do not find evidence for smaller parsec-scale structures in the absorbing gas, although this may simply be an issue of resolution. Variable components of the source at 21-cm may be significantly more extended than at mm-wavelengths, effectively not resolving small-scale variations in the H I opacity. Unfortunately, the source is significantly scatter broadened by the Galactic ISM at cm-wavelengths (Jones et al. 1996) and so it is difficult to directly measure the size seen by the absorber. Assuming that the core is emitting in the optically thick regime, we scale the $\sim 100 \mu\text{s}$ measured by Jin et al. (2003) at 43 GHz by $r \propto \nu^{-0.83}$ to estimate a typical scale ~ 3 mas (~ 20 pc at $z = 0.886$) for changes in the magnified core at 753 MHz. We do, however, caution that the time sampling and sensitivity of the current H I data are limited and our understanding of this system would be significantly improved by additional frequent monitoring of this source over the next 5 yr with either ASKAP or a radio telescope of similar capability.

3.3.4 Limits on the absorbing structure from ISS

In addition to the approximately yearly variability driven by changes in the flux density of the background source, the presence of sufficiently small-scale ($\lesssim 1$ mas) structure in the absorbing medium could drive stochastic fluctuations in the H I EW on time-scales of several months (and even years), due to scintillations associated with the turbulent ISM of the Milky Way (Macquart 2005). This variability is caused by the response of ISS to the presence of small-scale structure imprinted on the image of the absorbed source, and may therefore be evident even if the background source is not sufficiently compact to scintillate itself. The presence (or absence) of variability due to ISS can therefore be used to constrain the sizes and distribution of absorbing H I structures in the intervening galaxy. In the direction of PKS B1830–211, the NE2001 scattering model of the Galactic ISM by Cordes & Lazio (2002) predicts that the angular scale probed by refractive ISS is $\theta_{\text{ref}} = 2.1$ mas at the observed H I frequency of 753 MHz. The corresponding predicted point-source modulation index (i.e. the rms of the variations normalized by the mean flux density), due to refractive scintillation, is $m_{\text{pt}} = 12$ per cent and the predicted time-scale is $710 \nu_{30} \text{ d}$, where ν_{30} is the speed of the ISM transverse to the line of sight normalized to 30 km s^{-1} .

At the redshift of the absorbing system, refractive scintillation is sensitive to absorbing H I structure on linear scales less than

approximately 16 pc. If a single absorbing cloud of size θ_S were present across the extent of the background source, the optical depth of the absorption line would exhibit apparent variations with a modulation index of m_{pt} if $\theta_S < \theta_{\text{ref}}$ or $m_{\text{pt}}(\theta_{\text{ref}}/\theta_S)$ otherwise. However, if the background source is large relative to the typical cloud size, then it is more likely that N absorbing clouds are present across the extent of the source, and the modulation index would be reduced by a factor of $\sim N^{1/2}$ as the individual variations due to each absorbing system add incoherently with those of other clouds.

In Fig. 8, we showed the probability of residual stochastic variability in the EW data, once the yearly time-scale continuum variability has been taken into account. Assuming our model for continuum-driven variability, we obtain a 99.7 per cent (3σ) upper limit of approximately 6 per cent on any residual variability due to ISS. This limit implies that the characteristic scale of the H I absorbing structure exceeds approximately 38 pc across each lensed component, consistent with the conclusions reached in the previous subsection. Another possible scenario is that the scintillations are instead quenched by the contributions of many absorbing structures across the angular extent of the lensed image. In which case, refractive scintillations associated with any one absorbing cloud are diluted by the independent variations associated with other clouds. The present limit on optical depth variations therefore implies that six or more compact structures of size $\lesssim 16$ pc need to be present to reduce the modulation index of the optical depth variations below a detectable level. The foregoing limits apply if the range of velocities spanned by the absorbing clouds is comparable to the EW, v_{EW} , or if all the clouds that contribute to the observed absorption are contained within an angular scale θ_{ref} .

If the absorbing clouds span a velocity range small compared to the EW then the variations in the individual spectral lines that comprise the ensemble absorption spectrum would fluctuate independently, and so reduce the overall amplitude of the variations in the EW provided the clouds are distributed across a region exceeding θ_{ref} , and are correlated neither in velocity nor space. Denoting Δv as the velocity range over which scintillations are completely independent between sets of absorbing clouds, the amplitude of the variations is reduced by a factor $\sim \sqrt{(v_{\text{EW}}/\Delta v)}$, since their contributions would sum together incoherently. In other words, the contribution of several clouds at different velocities reduces the same variability in the same manner that an extended spatial distribution of clouds does. To this end, the lower limit on the number of compact clouds contributing to the opacity variations remains the same.

We note further that any stochastic variability due to scintillation would also imply variations in the NE/SW EW ratio, and the limit on the variation of this ratio places a similar limit on the contribution of scintillations to the variability.

4 MG J0414+0534

MG J0414+0534 is a heavily dust-reddened quasar at $z = 2.639 \pm 0.002$ (Lawrence et al. 1995), which is gravitationally lensed into four image components (Hewitt et al. 1992) by a foreground early-type galaxy at 0.9584 ± 0.0002 (Tonry & Kochanek 1999) and possibly a second ‘Object X’ at unknown redshift (Schechter & Moore 1993; Angonin-Willaime et al. 1994; Falco, Lehar & Shapiro 1997). Notably this quasar hosts the most distant and luminous water maser ever discovered, consistent with an extremely dusty and gas-rich host galaxy (Impellizzeri et al. 2008), which is further corroborated by the presence of H I absorption (Moore, Carilli & Menten 1999). The mid-infrared and radio flux ratios

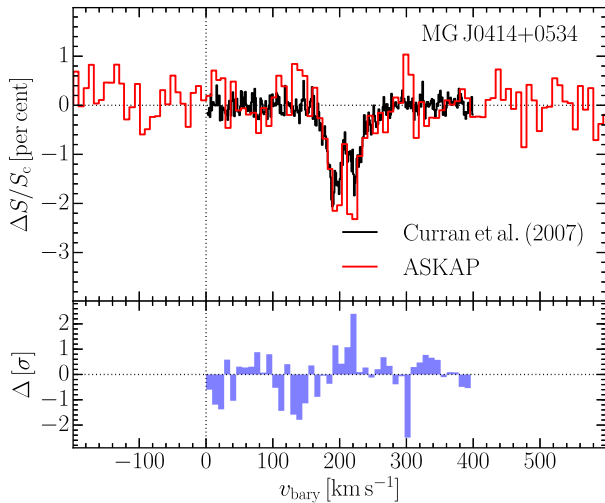


Figure 9. Spectra from ASKAP BETA (this work) and GBT (Curran et al. 2007) showing H I absorption associated with the early-type lensing galaxy at $z = 0.9584$ towards MG J0414+0534. The difference spectrum (blue filled) is shown in the bottom panel.

between the brightest components of the image are found to be anomalous when considering just a simple model of the lens, consisting of only the early-type galaxy and Object X components. This implies that several undiscovered components for the lens may exist, either in the form of satellite sub-haloes at the redshift of the early-type galaxy (e.g. Minezaki et al. 2009; MacLeod et al. 2013) or as intervening line-of-sight sub-structure (e.g. Inoue & Takahashi 2012; Inoue 2015). Therefore, detections of intervening galaxies through line-of-sight absorbing H I gas may provide useful constraints for selecting between these models.

Using the Green Bank Telescope (GBT), Curran et al. (2007) discovered H I absorption at the redshift of the early-type lensing galaxy. They speculated that the anomalous $\sim 200 \text{ km s}^{-1}$ velocity offset with respect to system redshift of $z = 0.9584 \pm 0.0002$ may arise from gas that is accreting on to the galaxy. Alternatively, the gas may be associated with a separate satellite galaxy at the same redshift, which has not yet been identified in either the optical or IR data. We also detected this line with ASKAP BETA, and find the spectrum to be consistent (albeit at much lower spectral resolution) with the velocity components originally identified by Curran et al. (see Fig. 9). However, we did not detect any of the other H I absorbers previously reported in the literature. We find that the system at $z = 0.379$, reported by Curran et al. (2011) as a possible counterpart to the putative Object X, is completely obscured by 1030 MHz RFI caused by the secondary surveillance radar uplink frequency used in air traffic control services worldwide. Given the ubiquity of this RFI signal at other observatory sites, we suspect that the original detection using the GBT may have been confused with a negative residual feature generated from RFI during the standard practice of single-dish on–off switching. We also did not detect the 21-cm absorbers reported by Tanna et al. (2013) at $z = 0.339$ and $z = 0.534$, which are expected to have peak optical depths of 0.6 and 0.45, respectively. We do not see any detectable RFI in our data at these frequencies⁷ and the optical depth sensitivity ($\sigma_\tau \sim 0.005$ in a single 18.5 kHz channel) is sufficient for detection. Based on our results we conclude that there is no evidence for further intervening

⁷ This could simply be the result of differences in the radio frequency environments of the two observatories.

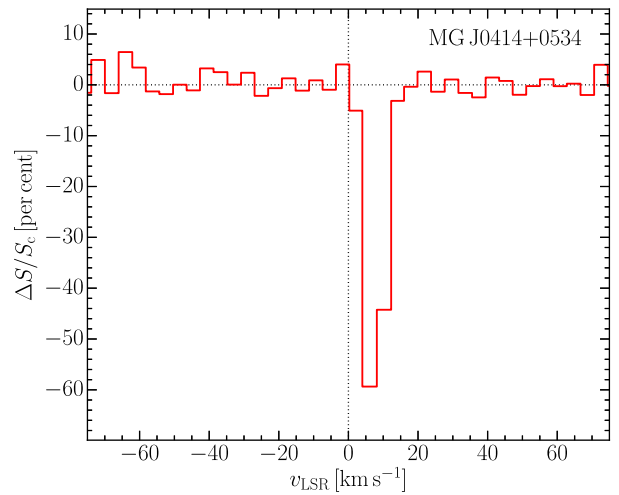


Figure 10. ASKAP BETA spectrum showing Galactic H I absorption towards MG J0414+0534.

H I absorbers at $z \leq 1$, beyond that associated with the known lensing galaxy at $z = 0.958$.

Apart from clarifying the extragalactic sight line towards MG J0414+053, we also detected H I absorption associated with the Milky Way. In Fig. 10, we show a section of the ASKAP BETA spectrum centred on the LSR frame. At $b = -31^\circ$ and $l = 187^\circ$, the quasar line-of-sight is positioned somewhat out of the plane and towards the Galactic anti-centre. The LSR velocity of the peak absorption ($\approx +5 \text{ km s}^{-1}$) is consistent with this direction through the Galactic plane. The narrow line width, and lack of significant sub-structure compared with the PKS B1830–211 line, is also consistent with a shorter path length through the H I disc of the Galaxy.

5 THE EXPECTED FREQUENCY OF INTERVENING ABSORBERS

A primary goal of future broad-band wide-field 21-cm surveys for intervening absorption will be to measure the cosmological H I mass density between $z \sim 0.2$ and 1.7, enabling direct comparison of the evolution of atomic gas in galaxies with that of the global star formation rate and molecular mass density (e.g. Kanekar & Briggs 2004; Morganti et al. 2015). Although the mass density of atomic gas in DLAs has been measured at these redshifts using the *HST*, the sample sizes are small and possibly subject to selection bias (Rao et al. 2006; Neeleman et al. 2016). The first attempt to demonstrate the feasibility of measuring the atomic mass density with a genuinely radio-selected 21-cm absorption survey was carried out by Darling et al. (2011) (see also Darling et al. 2004). Using pilot data from the Arecibo Legacy Fast Arecibo L-band Feed Array (ALFALFA) survey, Darling et al. (2011) were able to obtain an upper limit to the H I column density frequency distribution at low redshift ($z \lesssim 0.06$) that was consistent with the distribution measured by Zwaan et al. (2005) from 21-cm emission in a sample of nearby galaxies.

The substantial redshift interval covered by the ASKAP BETA data towards PKS B1830–211 and MG J0414+0534 allows us to carry out a test of whether the number of detected intervening absorbers is consistent with current measurements of the column density frequency distributions at low and high redshift. We follow the method of A15 to calculate the expected number of intervening systems of a given H I column density. Over the redshift range

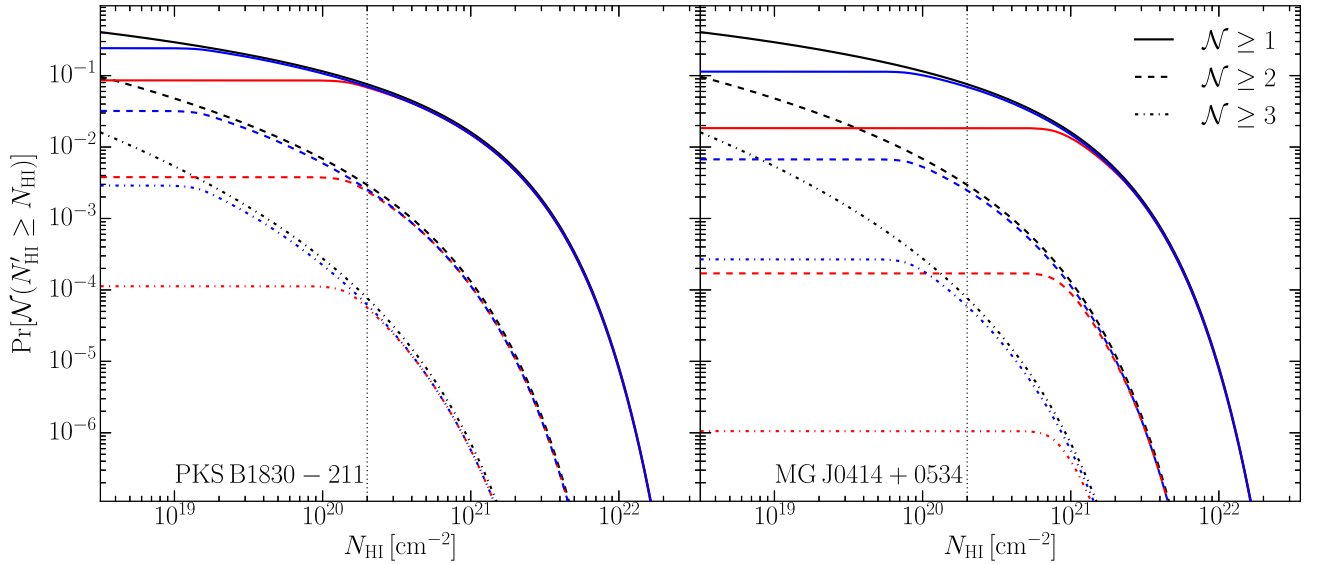


Figure 11. The probability of \mathcal{N} or more intervening H I systems occurring along a single random sight line between $z = 0$ and 1, where the black lines denote the cumulative distribution as a function of H I column density based on 21-cm emission and DLA surveys. The blue and red lines denote the probability of detection in our averaged ASKAP BETA data for spin temperatures of 100 and 1000 K, respectively. We use a simple Gaussian velocity model for the absorbing H I gas, assuming a line FWHM of 50 km s⁻¹ and a covering factor of unity. The vertical dotted line represents the minimum column density that defines a DLA.

covered by our data, we interpolate between the analytical Γ -functions for the column density distribution measured from 21-cm emission in the nearby Universe (Zwaan et al. 2005) and DLAs at $z \sim 3$ (Noterdaeme et al. 2009), extrapolating to lower column densities. Using the expected number of detections, we calculate the Poisson probability of \mathcal{N} or more intervening H I systems intercepting a single random sight line at redshifts between 0 and 1. We then adopt a simple Gaussian velocity model for the absorbing H I gas to calculate the column density sensitivity of our ASKAP BETA spectra (as shown in Figs 1 and 2) and hence estimate the probability of detecting \mathcal{N} or more absorbers towards PKS B1830–211 and MG J0414+0534. In our model, we assume an FWHM line width equal to 50 km s⁻¹ (equal to the typical widths seen in the detections towards these quasars), a covering factor of 1, and a spin temperature in the typical range of 100–1000 K.

The resulting probability distributions, as a cumulative function of column density, are shown in Fig. 11. If our sight lines were randomly chosen, we could simply test our detection yields against these estimated probabilities. However, given that we selected our sources based on the knowledge that they are strongly gravitationally lensed by at least one intervening gas-rich galaxy, within the redshift range covered by our data, we should ignore the primary lensing galaxy in our analysis. With this in mind, the detection yield in the case of PKS B1830–211 is one intervening absorber, while for MG J0414+0534 it is zero. Both cases, while not hugely constraining, are entirely consistent with that expected from our current understanding of the H I content of the Universe. We estimate that the probability of detecting two or more absorbers towards PKS B1830–211 is less than about 3 per cent, which seems consistent with the absence of any new detections towards this system. With an estimated probability of less than 0.03 per cent, we agree with Tanna et al. (2013) that the probability of detecting three or more intervening absorbers towards MG J0414+0534 (in addition to the lensing galaxy) is very unlikely. Our falsification of these original detections is therefore consistent with expectations.

6 CONCLUSIONS

We have carried out a wide-band 21-cm study of the lensed radio quasars PKS B1830–211 and MG J0414+0534 using commissioning data from the Boolardy Engineering Test Array of the Australian SKA Pathfinder. Our data allowed us to survey these sight lines for cold gas revealed by H I and OH absorption over an almost continuous redshift interval between $z_{\text{HI}} = 0$ and 1. We summarize our conclusions as follows.

- (i) Towards PKS B1830–211, we have re-detected H I and OH absorption associated with the $z = 0.886$ lens (Wiklind & Combes 1996; Chengalur et al. 1999) and the second absorber at $z = 0.193$ (Lovell et al. 1996). No further intervening galaxies were detected in this sight line over these redshifts.
- (ii) In the case of MG J0414+0534, we did not re-detect three of the intervening systems previously reported in the literature (Curran et al. 2011; Tanna et al. 2013), confirming only the H I absorber associated with the early-type gravitational lens at $z = 0.958$ (Curran et al. 2007). Given that our data are sufficiently sensitive to detect these lines, it is likely that the original identifications were mistakenly confused with RFI. We conclude that no H I counterparts have yet been found for the intervening sub-structures that could explain the observed flux ratio anomalies between image components.
- (iii) In the $z = 0.886$ lensing galaxy of PKS B1830–211, we find evidence of approximately yearly variability of a few per cent over the timeline spanned by the WSRT observations undertaken in 1997/1998 and our ASKAP BETA observations in 2014/2015. Variations in the H I EW are correlated with the total continuum flux density and appear to be coherent between the NE and SW images of the core. This behaviour arises naturally as a result of intrinsic variability in the compact core that is preferentially covered by the absorbing gas. We suggest that similar behaviour in absorption lines with several widely spaced velocity components detected in the 21-cm spectra of quasars could be used as a strong prior for selecting gravitationally lensed candidates.

(iv) The absence of any detectable variability in the ratio of H I EWs towards the NE and SW components, in contrast to that seen in the molecular absorption lines, suggests that the absorbing gas is distributed on scales larger than that probed by changes in the source structure. Higher cadence and S/N observations over the next 5 yr with ASKAP will be able to test for further changes in optical depth and provide more stringent constraints on this model and the physical size of the H I gas distribution.

(v) The absence of any detectable stochastic H I variability from ISS lends further evidence that opaque H I structures in the foreground galaxy are distributed on physical scales larger than approximately 40 pc.

(vi) Given the 21-cm optical depth sensitivity of our data, and assuming a simple Gaussian velocity model for the absorbing H I gas, we find that the number of intervening systems detected towards both PKS B1830–211 and MG J0414+0534 is consistent with the column density frequency distribution functions measured from local 21-cm and high-*z* DLA surveys.

ACKNOWLEDGEMENTS

JRA thanks Ron Ekers, Paolo Serra, Ger de Bruyn, and Naomi McClure-Griffiths for useful discussions on interpretation, Ryan Shannon and David Parkinson for advice and comments on the statistical analysis, and Jim Lovell for providing digital versions of his published spectra. We also thank Sebastien Muller and the anonymous referee for comments that helped improve this paper.

The Australian SKA Pathfinder is part of the Australia Telescope National Facility which is managed by CSIRO. Operation of ASKAP is funded by the Australian Government with support from the National Collaborative Research Infrastructure Strategy. Establishment of the Murchison Radio-astronomy Observatory was funded by the Australian Government and the Government of Western Australia. ASKAP uses advanced supercomputing resources at the Pawsey Supercomputing Centre. We acknowledge the Wajarri Yamatji people as the traditional owners of the Observatory site.

JRA acknowledges support from a Bolton Fellowship. Parts of this research were conducted by the Australian Research Council Centre of Excellence for All-sky Astrophysics (CAASTRO), through project number CE110001020. We have made use of *ASTROPY*, a community-developed core *PYTHON* package for astronomy (Astropy Collaboration et al. 2013); the NASA/IPAC Extragalactic Database (NED) which is operated by the Jet Propulsion Laboratory, California Institute of Technology, under contract with the National Aeronautics and Space Administration; NASA's Astrophysics Data System Bibliographic Services; and the VizieR catalogue access tool operated at CDS, Strasbourg, France.

REFERENCES

Abdo A. A. et al., 2015, *ApJ*, 799, 143
 Allison J. R., Sadler E. M., Whiting M. T., 2012, *PASA*, 29, 221
 Allison J. R., Sadler E. M., Meekin A. M., 2014, *MNRAS*, 440, 696
 Allison J. R. et al., 2015, *MNRAS*, 453, 1249 (A15)
 Angonin-Willaime M.-C., Vanderriest C., Hammer F., Magain P., 1994, *A&A*, 281, 388
 Astropy Collaboration et al., 2013, *A&A*, 558, A33
 Barnacka A., Glicenstein J.-F., Moudou Y., 2011, *A&A*, 528, L3
 Barnacka A., Geller M. J., Dell'Antonio I. P., Benbow W., 2015, *ApJ*, 809, 100
 Biggs A. D., Zwaan M. A., Hatziminaoglou E., Péroux C., Liske J., 2016, *MNRAS*, 462, 2819

Borthakur S., Momjian E., Heckman T. M., York D. G., Bowen D. V., Yun M. S., Tripp T. M., 2014, *ApJ*, 795, 98
 Braun R., 2012, *ApJ*, 749, 87
 Briggs F. H., 1983, *ApJ*, 274, 86
 Brogan C. L., Zauderer B. A., Lazio T. J., Goss W. M., DePree C. G., Faison M. D., 2005, *AJ*, 130, 698
 Buchner J. et al., 2014, *A&A*, 564, A125
 Burgarella D. et al., 2013, *A&A*, 554, A70
 Carilli C. L., Walter F., 2013, *ARA&A*, 51, 105
 Catinella B., Cortese L., 2015, *MNRAS*, 446, 3526
 Chang T.-C., Pen U.-L., Bandura K., Peterson J. B., 2010, *Nature*, 466, 463
 Chengalur J. N., de Bruyn A. G., Narasimha D., 1999, *A&A*, 343, L79
 Cohen R. D., Smith H. E., Junkkarinen V. T., Burbidge E. M., 1987, *ApJ*, 318, 577
 Condon J. J., Cotton W. D., Greisen E. W., Yin Q. F., Perley R. A., Taylor G. B., Broderick J. J., 1998, *AJ*, 115, 1693
 Cordes J. M., Lazio T. J. W., 2002, preprint ([arXiv:astro-ph/0207156](https://arxiv.org/abs/astro-ph/0207156))
 Courbin F., Meylan G., Kneib J.-P., Lidman C., 2002, *ApJ*, 575, 95
 Crighton N. H. M. et al., 2015, *MNRAS*, 452, 217
 Curran S. J., Darling J., Bolatto A. D., Whiting M. T., Bignell C., Webb J. K., 2007, *MNRAS*, 382, L11
 Curran S. J., Whiting M. T., Tanna A., Bignell C., Webb J. K., 2011, *MNRAS*, 413, L86
 Darling J., Giovanelli R., Haynes M. P., Bolatto A. D., Bower G. C., 2004, *ApJ*, 613, L101
 Darling J., Macdonald E. P., Haynes M. P., Giovanelli R., 2011, *ApJ*, 742, 60
 Deshpande A. A., 2000, *MNRAS*, 317, 199
 Dickey J. M. et al., 2013, *PASA*, 30, e003
 Donnarumma I. et al., 2011, *ApJ*, 736, L30
 Dutta P., Chengalur J. N., Roy N., Goss W. M., Arjunwadkar M., Minter A. H., Brogan C. L., Lazio T. J. W., 2014, *MNRAS*, 442, 647
 Dutta R., Gupta N., Srianand R., O'Meara J. M., 2016, *MNRAS*, 456, 4209
 Falco E. E., Lehar J., Shapiro I. I., 1997, *AJ*, 113, 540
 Fernández X. et al., 2016, *ApJ*, 824, L1
 Feroz F., Hobson M. P., 2008, *MNRAS*, 384, 449
 Feroz F., Hobson M. P., Bridges M., 2009, *MNRAS*, 398, 1601
 Feroz F., Hobson M. P., Cameron E., Pettitt A. N., 2013, preprint ([arXiv:1306.2144](https://arxiv.org/abs/1306.2144))
 Frye B., Welch W. J., Broadhurst T., 1997, *ApJ*, 478, L25
 Garrett M. A., Nair S., Porcas R. W., Patnaik A. R., 1997, *Vistas Astron.*, 41, 281
 Garrett M. A., Leppanen K., Porcas R. W., Patnaik A. R., Nair S., Terasranta H., 1998, in Zensus J. A., Taylor G. B., Wrobel J. M., eds, *ASP Conf. Ser. Vol. 144, IAU Colloq. 164: Radio Emission from Galactic and Extragalactic Compact Sources*. Astron. Soc. Pac., San Francisco, p. 313
 Giovanelli R., Haynes M. P., 2016, *A&AR*, 24, 1
 Goss W. M., Richards A. M. S., Muxlow T. W. B., Thomasson P., 2008, *MNRAS*, 388, 165
 Gunawardhana M. L. P. et al., 2013, *MNRAS*, 433, 2764
 Gupta N., Srianand R., Petitjean P., Bergeron J., Noterdaeme P., Muzahid S., 2012, *A&A*, 544, A21
 Heckman T. M., Best P. N., 2014, *ARA&A*, 52, 589
 Hewitt J. N., Turner E. L., Lawrence C. R., Schneider D. P., Brody J. P., 1992, *AJ*, 104, 968
 Hopkins A. M., Beacom J. F., 2006, *ApJ*, 651, 142
 Hotan A. W. et al., 2014, *PASA*, 31, e041
 Impellizzeri C. M. V., McKean J. P., Castangia P., Roy A. L., Henkel C., Brunthaler A., Wucknitz O., 2008, *Nature*, 456, 927
 Inoue K. T., 2015, *MNRAS*, 447, 1452
 Inoue K. T., Takahashi R., 2012, *MNRAS*, 426, 2978
 Jauncey D. L. et al., 1991, *Nature*, 352, 132
 Jin C., Garrett M. A., Nair S., Porcas R. W., Patnaik A. R., Nan R., 2003, *MNRAS*, 340, 1309
 Johnston S., Koribalski B., Wilson W., Walker M., 2003, *MNRAS*, 341, 941
 Johnston S. et al., 2007, *PASA*, 24, 174
 Jones D. L. et al., 1996, *ApJ*, 470, L23

- Kanekar N., Briggs F. H., 2004, *New Astron. Rev.*, 48, 1259
- Kanekar N., Chengalur J. N., 2001, *MNRAS*, 325, 631
- Kanekar N., Sethi S., Dwarakanath K. S., 2016, *ApJ*, 818, L28
- Kennicutt R. C., Jr, 1998, *ApJ*, 498, 541
- Keres D., Yun M. S., Young J. S., 2003, *ApJ*, 582, 659
- Kochanek C. S., Narayan R., 1992, *ApJ*, 401, 461
- Koopmans L. V. E., de Bruyn A. G., 2005, *MNRAS*, 360, L6
- Lagos C. D. P., Baugh C. M., Zwaan M. A., Lacey C. G., Gonzalez-Perez V., Power C., Swinbank A. M., van Kampen E., 2014, *MNRAS*, 440, 920
- Lah P. et al., 2007, *MNRAS*, 376, 1357
- Lane W. M., Briggs F. H., Smette A., 2000, *ApJ*, 532, 146
- Lawrence C. R., Elston R., Januzzi B. T., Turner E. L., 1995, *AJ*, 110, 2570
- Lazio T. J. W., Brogan C. L., Goss W. M., Stanimirović S., 2009, *AJ*, 137, 4526
- Lewis G. F., Ibata R. A., 2003, *MNRAS*, 340, 562
- Lidman C., Courbin F., Meylan G., Broadhurst T., Frye B., Welch W. J. W., 1999, *ApJ*, 514, L57
- Lovell J. E. J. et al., 1996, *ApJ*, 472, L5
- Lovell J. E. J., Jauncey D. L., Reynolds J. E., Wieringa M. H., King E. A., Tzioumis A. K., McCulloch P. M., Edwards P. G., 1998, *ApJ*, 508, L51
- McConnell D. et al., 2016, *PASA*, 33, e042
- MacLeod C. L., Jones R., Agol E., Kochanek C. S., 2013, *ApJ*, 773, 35
- McMullin J. P., Waters B., Schiebel D., Young W., Golap K., 2007, in Shaw R. A., Hill F., Bell D. J., eds, *ASP Conf. Ser. Vol. 376, Astronomical Data Analysis Software and Systems XVI*. Astron. Soc. Pac., San Francisco, p. 127
- Macquart J.-P., 2005, *A&A*, 433, 827
- Martí-Vidal I. et al., 2013, *A&A*, 558, A123
- Martin A. M., Papastergis E., Giovanelli R., Haynes M. P., Springob C. M., Stierwalt S., 2010, *ApJ*, 723, 1359
- Masui K. W. et al., 2013, *ApJ*, 763, L20
- Minezaki T., Chiba M., Kashikawa N., Inoue K. T., Kataza H., 2009, *ApJ*, 697, 610
- Moore C. B., Carilli C. L., Menten K. M., 1999, *ApJ*, 510, L87
- Morganti R., Sadler E. M., Curran S., 2015, in Bourke T. et al., eds, *Proc. Sci., Cool Outflows and HI Absorbers with SKA*. SISSA, Trieste, PoS(AASKA14)134
- Muller S., Guélin M., 2008, *A&A*, 491, 739
- Muller S. et al., 2011, *A&A*, 535, A103
- Muller S. et al., 2013, *A&A*, 551, A109
- Muller S. et al., 2014, *A&A*, 566, A112
- Nair S., Narasimha D., Rao A. P., 1993, *ApJ*, 407, 46
- Nair S., Jin C., Garrett M. A., 2005, *MNRAS*, 362, 1157
- Neeleman M., Prochaska J. X., Ribaud J., Lehner N., Howk J. C., Rafelski M., Kanekar N., 2016, *ApJ*, 818, 113
- Noterdaeme P., Petitjean P., Ledoux C., Srianand R., 2009, *A&A*, 505, 1087
- Noterdaeme P. et al., 2012, *A&A*, 547, L1
- Offringa A. R., de Bruyn A. G., Biehl M., Zaroubi S., Bernardi G., Pandey V. N., 2010, *MNRAS*, 405, 155
- Purcell C. R. et al., 2015, *ApJ*, 804, 22
- Rao A. P., Subrahmanyan R., 1988, *MNRAS*, 231, 229
- Rao S. M., Turnshek D. A., Nestor D. B., 2006, *ApJ*, 636, 610
- Reid M. J. et al., 2014, *ApJ*, 783, 130
- Reynolds J., 1994, AT Technical Document AT/39.3/040.
- Rhee J., Lah P., Chengalur J. N., Briggs F. H., Colless M., 2016, *MNRAS*, 460, 2675
- Roy N., Chengalur J. N., Dutta P., Bharadwaj S., 2010, *MNRAS*, 404, L45
- Roy N., Minter A. H., Goss W. M., Brogan C. L., Lazio T. J. W., 2012, *ApJ*, 749, 144
- Sánchez-Ramírez R. et al., 2016, *MNRAS*, 456, 4488
- Sault R. J., Teuben P. J., Wright M. C. H., 1995, in Shaw R. A., Payne H. E., Hayes J. J. E., eds, *ASP Conf. Ser. Vol. 77, Astronomical Data Analysis Software and Systems IV*. Astron. Soc. Pac., San Francisco, p. 433
- Schechter P. L., Moore C. B., 1993, *AJ*, 105, 1
- Schinkel A. E., Bunton J. D., Cornwell T. J., Feain I., Hay S. G., 2012, *Proc. SPIE*, 8444, 84442A
- Schmidt M., 1959, *ApJ*, 129, 243
- Schulz A., Henkel C., Menten K. M., Muller S., Muders D., Bagdonaite J., Ubachs W., 2015, *A&A*, 574, A108
- Serra P. et al., 2015, *MNRAS*, 452, 2680
- Sobral D., Smail I., Best P. N., Geach J. E., Matsuda Y., Stott J. P., Cirasuolo M., Kurk J., 2013, *MNRAS*, 428, 1128
- Srianand R., Gupta N., Rahmani H., Momjian E., Petitjean P., Noterdaeme P., 2013, *MNRAS*, 428, 2198
- Subrahmanyan R., Narasimha D., Pramesh-Rao A., Swarup G., 1990, *MNRAS*, 246, 263
- Subrahmanyan R., Kesteven M. J., te Lintel Hekkert P., 1992, *MNRAS*, 259, 63
- Tanna A., Curran S. J., Whiting M. T., Webb J. K., Bignell C., 2013, *ApJ*, 772, L25
- Tonry J. L., Kochanek C. S., 1999, *AJ*, 117, 2034
- Tuthill J., Hampson G., Bunton J., Brown A., Neuhold S., Bate-man T., de Souza L., Joseph J., 2012, Development of Multi-stage Filter Banks for ASKAP. IEEE. Available at: <http://ieeexplore.ieee.org/document/6328788>
- Wiklind T., Combes F., 1996, *Nature*, 379, 139
- Wiklind T., Combes F., 1998, *ApJ*, 500, 129
- Wiklind T., Combes F., 2001, in Brainerd T. G., Kochanek C. S., eds, *ASP Conf. Ser. Vol. 237, Gravitational Lensing: Recent Progress and Future Go*. Astron. Soc. Pac., San Francisco, p. 155
- Winn J. N., Kochanek C. S., McLeod B. A., Falco E. E., Impey C. D., Rix H.-W., 2002, *ApJ*, 575, 103
- Wolfe A. M., Briggs F. H., Davis M. M., 1982, *ApJ*, 259, 495
- Wolfe A. M., Gawiser E., Prochaska J. X., 2005, *ARA&A*, 43, 861
- Zafar T., Péroux C., Popping A., Milliard B., Deharveng J.-M., Frank S., 2013, *A&A*, 556, A141
- Zwaan M. A., van der Hulst J. M., Briggs F. H., Verheijen M. A. W., Ryan-Weber E. V., 2005, *MNRAS*, 364, 1467
- Zwart J. T. L., Jarvis M. J., Deane R. P., Bonfield D. G., Knowles K., Madhanpall N., Rahmani H., Smith D. J. B., 2014, *MNRAS*, 439, 1459

This paper has been typeset from a \LaTeX file prepared by the author.